3D printing of calcined clay-limestone-based cementitious materials

Chen, Yu; He, Shan ; Zhang, Yu; Wan, Zhi; Copuroglu, Oguzhan; Schlangen, Erik

DOI
10.1016/j.cemconres.2021.106553

Publication date
2021

Document Version
Final published version

Published in
Cement and Concrete Research

Cement and Concrete Research 149 (2021) 106553

Contents lists available at ScienceDirect

Cement and Concrete Research

journal homepage: www.elsevier.com/locate/cemconres

3D printing of calcined clay-limestone-based cementitious materials

Yu Chen *, Shan He, Yu Zhang, Zhi Wan, Oğuzhan Çopuroğlu, Erik Schlangen

Microlab, Faculty of Civil Engineering and Geosciences, Delft University of Technology, Delft, the Netherlands

ARTICLE INFO

Keywords:
3D concrete printing
Calcined clay
Sustainable cementitious material
Early-age hydration
Stiffness evolution

ABSTRACT

This paper aims to investigate the influences of high Portland cement substitutions (>60 wt%) by low-grade calcined clay (CC) and limestone (LF) on 3D concrete printability, stiffness evolution and early-age hydration. Results show that, with the same dosage of admixtures (superplasticizer and viscosity modifier), increasing LF and CC content reduced the slump, flowability and initial material flow rate, and significantly improved the buildability of fresh mixtures, which can be attributed to the reduced water film thickness (WFT). Furthermore, the stiffness evolution and SSA_{total} development up to the first 3 h were accelerated by increasing CC content, which can also be linked to the change of WFT, and consumption of superplasticizer for the dispersion induced by hydration products. Additionally, the dilution effect on compressive strength and hydration caused by the high cement replacement was observed.

1. Introduction

The past decade has seen the rapid development of 3D printing research in building and construction industry. 3D concrete printing, being one of the emerging technologies, has attracted great interest from academia and industry [1–4]. To date, 3D printing of concrete can be classified into three main categories, including material extrusion (e.g., contour crafting), material jetting, and particle-bed binding (e.g., D-shape) [5]. Extrusion-based 3D concrete printing (3DCP) that employs a continuous filament extrusion and a layer-wise process for forming objects without formwork is by far the most exploited technology [2,6] due to its potential to be applied in large-scale on-site construction [7,8]. However, the development of the extrusion-based 3DCP was challenged by its stringent requirements on the material, i.e., sufficient flowability during pumping and extrusion, as well as zero-slump and high stiffness after deposition [4,9].

Extrusion of high or sufficiently stiff materials, as one of the most common 3DCP strategies summarized by Mechtcherine et al. [5], is used in this study. To develop such cementitious materials, fresh-state behaviors, including pumpability, extrudability, open time, and buildability have to be characterized [7,10–12]. The pumping and extrusion can be considered as a single process if the extrusion force is only supplied by the pump without any additional energy input. In this study, pumpability and extrudability were combined as one material property defined as the ability of tested material to be continuously delivered and printed with an acceptable quality [11,13,14]. Since the workability of fresh cementitious materials changes with time, open time, also known as printability window [14], is proposed to describe the timespan during which a mixture can maintain its extrudability [2,12,15]. Lastly, buildability refers to the ability of a freshly printed material to retain the layered shape against the gradually increasing deadweight of upper layers [4,12]. All these aforementioned material features for 3D printing can be either directly evaluated by inline printing methods (inline tests represent the experiments conducted using a 3DCP setup), as proposed by studies [4,7,11,14,16,17], or indirectly quantified by offline methods, i.e., ram extrusion test [7,18–21], (rheometer based) constant shear rate [17,22] or hysteresis loop test [23–30], and slump and slump-flow (flow table) tests [4,16,31]. While most of inline printing tests may be accompanied by massive material consumption and intensive labor works, offline methods are more efficient and thus more appropriate at the initial stage of new material development.

Until now, in most of proposed 3D printable cementitious materials, ordinary Portland cement (PC) still occupies a relatively high content (>330 kg/m^3), which partially neutralizes the sustainable benefits of 3DCP in aspects of formwork free and material-efficient designs [4,13,32]. Besides the absence of coarse aggregates, the low aggregate content in the material recipes for 3D printing is the major cause for its high PC% [32]. The aggregate to binder ratio (A/B) in the printable mixtures developed by studies [4,11,17,25,27,28,33–41] is smaller than 2, whereas the A/B is about 3–5 in mold-cast concrete and mortar with

* Corresponding author.
E-mail addresses: Y.Chen-6@tudelft.nl (Y. Chen), S.He-2@tudelft.nl (S. He), Y.Zhang-28@tudelft.nl (Y. Zhang), Z.Wan-1@tudelft.nl (Z. Wan), O.Copuroglu@tudelft.nl (O. Çopuroğlu), Erik.Schlangen@tudelft.nl (E. Schlangen).

https://doi.org/10.1016/j.cemconres.2021.106553
Received 18 March 2021; Received in revised form 14 June 2021; Accepted 21 July 2021
Available online 4 August 2021

the moderate or even high strength at 28 days [42]. The A/B in printable cementitious materials is limited by the 3DCP setup, i.e., the limited dimension of hose and pumping capability. Increasing A/B could significantly enhance the yield stress and plastic viscosity of fresh mixture [6,11,43], which results in a substantial burden on the pump. Hence, based on the current printing setup, reducing the PC amount by merely increasing the aggregate content seems challenging. Another solution, as pointed out by [44,45], is to partially replace PC with supplementary cementitious materials (SCMs).

Common SCMs, for instance, fly ash, silica fume, and blast furnace slag, have been employed as binders in many printable cementitious materials (see [6,11,19,36,39–41,46]). However, as the availability of these industrial by-products becomes increasingly unstable [4,7,44,47,48], alternative SCMs are needed in the long term. Considering their worldwide abundance and low CO_2 footprint during the material production [47,49–51], calcined clay and limestone are highlighted as the proper alternatives to conventional SCMs. As one of the promising sustainable cements, limestone calcined clay cement (LC3) has experienced a fast development over the past years [47,52,53]. The main reactive phase (reactive aluminates and silicates) in calcined clay is metakaolin (MK), which reacts with calcium hydroxide generated by cement hydration to form calcium-aluminosilicate-hydrates (C-A-S-H). Meanwhile, hemi/mono-carboaluminate is also generated via the reactions between calcite (provided by limestone) and alumina species in the pore solution [47–49,54,55]. These reactions reduce total capillary porosity, resulting in enhanced mechanical performance and durability of LC3-based concrete [47,49,56]. Besides, the use of calcined clay and limestone may also be beneficial for 3D printing. Earlier studies [57,58] showed that the LC3 paste displayed a much higher plastic viscosity, initial static and dynamic yield stresses, and structuration rate than the ordinary Portland cement paste. The increase in initial static yield stress can improve the shape retention properties and buildability of fresh mixtures [27]. The high structuration rate primarily promotes structural build-up (time-dependent static yield stress, see [59]) and stiffness evolution of deposited cementitious materials at rest, which could yield the high structural stability of a large object for a long printing time (3–4 h) [59,60].

On the contrary, the addition of calcined clay was reported to reduce the workability [61,62] and consequently increase the demand for mixing water and superplasticizer [63–65], which may be governed by the features of the used calcined clay, i.e., high content of reactive aluminate, fine particle size, high specific surface area (SSA), and layered particle structure. Nevertheless, the link between these material characteristics and fresh properties has not been systematically built. Furthermore, at present, the maximum content of PC substitution by a blend of limestone and calcined clay is 60 wt% (B60) for the mixtures employed in 3DCP. The influences of different dosages of viscosity modifying admixture addition and various grade levels of calcined clay on 3D printability, hydration and compressive strength of mixture B60 have been tailored by [4,7]. However, to our knowledge, there have been no attempts to formulate a printable mixture with a higher content (>60% of the binder mass) calcined clay and limestone for 3DCP. The impacts caused by increasing the proportion of limestone and calcined clay in the binder on 3D printability, fresh and hardened properties are not clear yet.

The goal of this study is to investigate the effect of high Portland cement substitutions (>60 wt%) by blends of calcined clay and limestone on 3D printability, stiffness evolution and early-age hydration. Slump, slump-flow, and water retention tests were performed at the beginning for developing the printable mixtures. Afterwards, the developed mixtures were assessed by using inline printing methods, i.e., extrudability and operation windows, and buildability tests. In addition, the impacts on stiffness development and early-age hydration were determined through measuring the initial setting time, shape stability under static load in the first 2 h, total specific surface areas at 1 h and 3 h, released reaction heat within the first 7 days and compressive strength of mold-cast samples at 1, 3, 7 and 28 days. Finally, a discussion of the obtained results, limitations and perspectives is given.

2. Material and methods

2.1. Materials

The binder of 3D printable mixtures in this study was comprised of CEM I 52.5R Portland cement (PC), limestone powder (LF), and calcined clay (CC). CC that contained about 50 wt% of metakaolin was supplied by Argeco, France. The particle size distribution of all these materials is illustrated in Fig. 1 (a), determined using laser diffractometry. Due to the presence of quartz impurity, CC shows the largest average particle size compared to other fines used in this study (see Fig. 2). The physical characteristics and oxide composition of all binding materials are presented in Table 1. The Brunauer-Emmett-Teller (BET) method using liquid nitrogen (N_2) was employed to measure the specific surface area (SSA) of PC, LF, and CC. It was found that CC showed a much higher SSA than other binding materials. The X-ray diffraction (XRD) pattern of CC is given in Fig. 1 (b). A PhilipsPW1830 powder X-ray diffractometer with Cu-Kα radiation operated at 45 kV and 40 mA was used to conduct XRD. Except for quartz, uncalcined kaolinite and mullite were also observed in CC. Besides, the reactive content of CC was measured via a chemical dissolution test based on NEN-EN 196-2 [66]. The total reactive content was about 48.8 wt% (12.3 wt% reactive silicate, 32.0 wt% reactive aluminite, and 4.5 wt% other reactive phases). Under secondary electron (SE) mode of scanning electron microscopy (SEM), the CC particles were observed to exhibit subhedral flaky habit and clustered structure (see Fig. 2), which might be the reason for its extremely high SSA. Fine quartz sand with a grain size of 0.125–2 mm, as shown in Fig. 1 (a), was employed as aggregate of the studied mixtures.

Table 2 presents the preliminary mixture compositions of 3D printable cementitious materials. The water-to-binder ratio (W/B) of 0.3 and sand-to-binder ratio (S/B) of 1.5 were kept identical in the current study. In mixtures B45, B75, and B90, PC was replaced by the blend of LF and CC in a mass ratio of 1:2 with different proportions. According to earlier studies [49,67], a limestone-to-calcined clay ratio of 1:2 may give the best compressive strength development compared to other mass ratios. In addition to these mixtures, the binder of mixture B0 contained only PC as a reference to investigate the influences of LF and CC on fresh state behaviors, cement hydration, and compressive strength. Note that the current mix designs in Table 2 could not be used for 3D printing directly. According to earlier studies [4,17,19,68], the addition of admixtures could help to modify the rheology of fresh mixtures for acceptable 3D printability. In this study, both polycarboxylate ether (PCE)-based superplasticizer (SP) and hydroxypropyl methylcellulose (HPMC)-based viscosity modifying admixture (VMA) were used. The proper dosages for such admixtures were determined via a series of trial-based tests in Section 2.2.1. All fresh mixtures (paste and mortar) were prepared in accordance with the mixing procedures as described in Table 3. The time of mixing liquid components (water and SP) with dry materials was defined as time zero ($t = 0$ min).

2.2. Test procedures

2.2.1. Formulation of printable mix designs

2.2.1.1. Slump and slump-flow tests. Owing to the simple test apparatus and protocol, slump and slump-flow tests seem to be the most appropriate methods to effectively reflect the printability of numerous fresh mixtures in a short period. The slump value is dependent on the static yield stress of the fresh mixture, which may indicate the corresponding shape retention or even buildability performance [31]. The flowability of fresh mixture determined by the slump-flow test is related to its pumpability and extrudability [16,31]. In this study, Hägermann cone

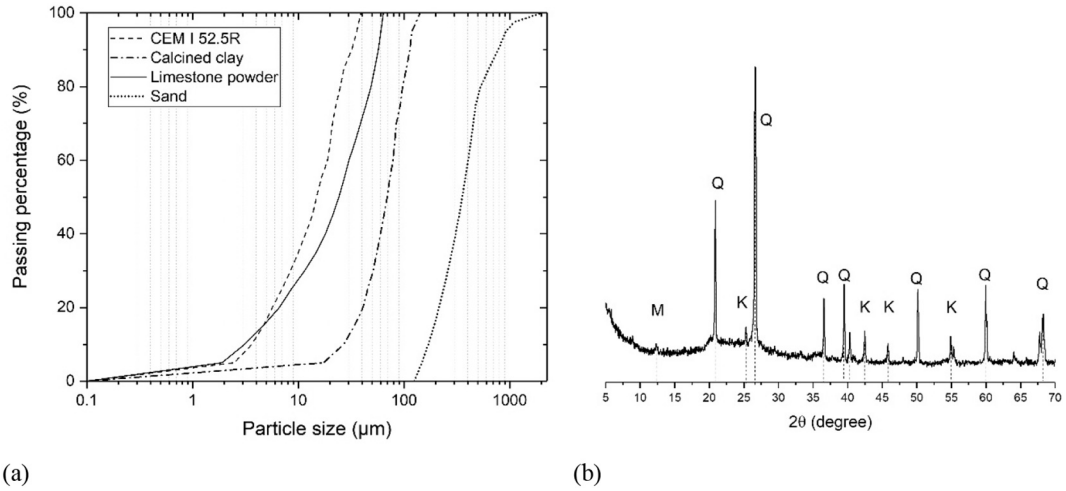

Fig. 1. (a) Particle size distribution of CEM I 52.5R Portland cement, calcined clay, limestone powder, and sand used in this paper. The particle size of sand was determined by using a sieving machine. The grain size of all binding materials was measured via laser diffractometry. (b) XRD (Cu-Kα radiation) pattern of calcined clay. M-mullite, Q-quartz, K-kaolinite.

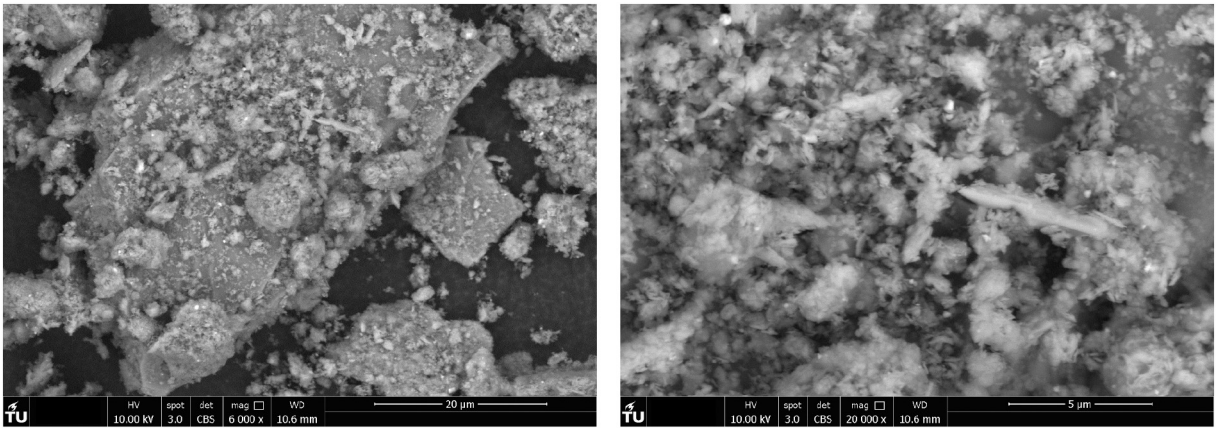

Fig. 2. Electron micrograph of calcined clay under secondary electron mode. Left: magnification of ×6000. Right: magnification of ×20,000.

Table 1
Physical properties and X-ray fluorescence spectrometry (XRF) composition of CEM I 52.5R Portland cement, limestone powder, and calcined clay.

	CEM I 52.5R Portland cement	Limestone powder	Calcined clay
Density [g/cm^3]	3.12	2.65	2.51
SSA [m^2/g]	1.16	1.22	10.06
D_{v50} [μm]	14.86	24.19	69.35
XRF [wt%]			
CaO	68.7	39.6	0.6
SiO_2	17.4	0.2	55.1
Al_2O_3	4.1	0	38.4
Fe_2O_3	2.8	0.1	2.6
K_2O	0.6	0	0.2
TiO_2	0.3	0	1.1
ZrO_2	0	0	0.1
Other	6.1	60.1	1.9
Total	100.0	100.0	100.0

(70 mm upper internal diameter, 100 mm bottom internal diameter, and 60 mm height) was employed to perform both slump and slump-flow tests. The slump-flow test is also known as Hägermann flow table test. The test procedures could refer to studies [4,31]. The inner surface of cone mold was lubricated by mold oil before filling the fresh mortar. For

Table 2
Preliminary mixture composition of cementitious materials (excluding admixtures).

	Binding material			Water	Aggregate
	Portland cement (wt %)	Calcined clay (wt%)	Limestone powder (wt%)	Water/binder (W/B)	Sand/binder (S/B)
B0	100	0	0	0.3	1.5
B45	55	30	15	0.3	1.5
B75	25	50	25	0.3	1.5
B90	10	60	30	0.3	1.5

Table 3
Mixing protocol for the fresh paste/mortar preparation.

Time [min:s]	Mixing procedures
−4:00	Mix dry blends at low speed by using a HOBART mixing machine
0:00	Add water and SP during mixing
2:00	Pause, scrape the bottom of bowl. Mix at high speed.
3:30	Pause, add VMA, and mix at low speed (for the mixture without VMA: stop, start to test/cast)
7:30	Pause, scrape the bottom of bowl. Mix at high speed.
10:00	Stop, start to test/cast.

the slump test, the height of the sample was measured after removal of the cone mold. However, if the sample could not retain its shape and the measured height was lower than 20 mm, the sample's height was recorded as 0 mm. After that, 25 times of table drops were conducted on the demolded sample within 25 s. By using a vernier caliper, the spread diameter was measured in four perpendicular directions. The average value of spread diameters was recorded as the result of slump-flow test. For each mixture, three repetitions were executed.

2.2.1.2. Water retention test. Under a specific pumping or extrusion pressure, the material must remain stable and homogenous to avoid pressurized bleeding and segregation, which may cause clogging of printing setup or adversely affect the material performances after extrusion [35]. Therefore, a proper water retention capacity of printable mixture is required. In this study, the water retention test was performed in accordance with ASTM C1506-09 [69]. The freshly mixed cementitious paste (about 15 min of material age) was weighed and filled in a Büchner funnel attached to a vacuum assembly. An ashless filter paper (20 μm sieve size, 110 mm diameter, Whatman™) was fixed between the paste and funnel. After exposing the apparatus to a vacuum condition for about 15 min, the loss of mixing water W_l was determined. The water retention capacity W_r of fresh paste can be calculated via Eq. (1).

$$W_r = \left(1 - \frac{W_l}{W_0}\right) \times 100\% \tag{1}$$

where W_0 denotes the mass of mixing water in the fresh paste.

2.2.2. Evaluation of 3D printability

2.2.2.1. 3DCP setup. For concrete/mortar printing, a lab-scale 3DCP setup at Delft University of Technology (TU Delft), introduced by earlier works [3,4,7], was employed in this study. As shown in Fig. 3, the 3DCP setup consisted of three primary components: a 3-degree of freedom Computer Numerical Control (CNC) system, a PFT Swing-M type material conveying pump, and a nozzle. The CNC machine can operate within an area of 1100 mm length, 720 mm width, and 290 mm height. The moving speed could be adjusted between 0 mm/min and 7200 mm/min. The material conveying pump (also known as progressive cavity pump) that provided primary forces for pumping and extrusion of fresh mixtures was based on a rotor and stator configuration. More details about the pump were given in Section 2.2.2.2. A 5 m material hose with an inner diameter of 25 mm was used to connect the pump and the nozzle. In this study, a down-flow nozzle with a round opening (diameter: 15 mm) was selected for performing the 3D printing test.

2.2.2.2. Extrudability and operation windows. The section of the material conveying pump is illustrated in Fig. 4 (a). Up to 38 L fresh mixtures can be filled in the hopper of the pump. Driving by the motor and rotor-stator system, the fresh mixture can be extruded at a specific flow rate (Q) constrained by both the motor speed and the rheology of fresh mixture. According to studies [4,34,38], the linear material flow rate (Q_{linear}) of fresh mixture should be near to the nozzle/printhead moving speed (V_n) for archiving an acceptable printing quality.

$$V_n = Q_{linear} = \frac{Q}{A} \tag{2}$$

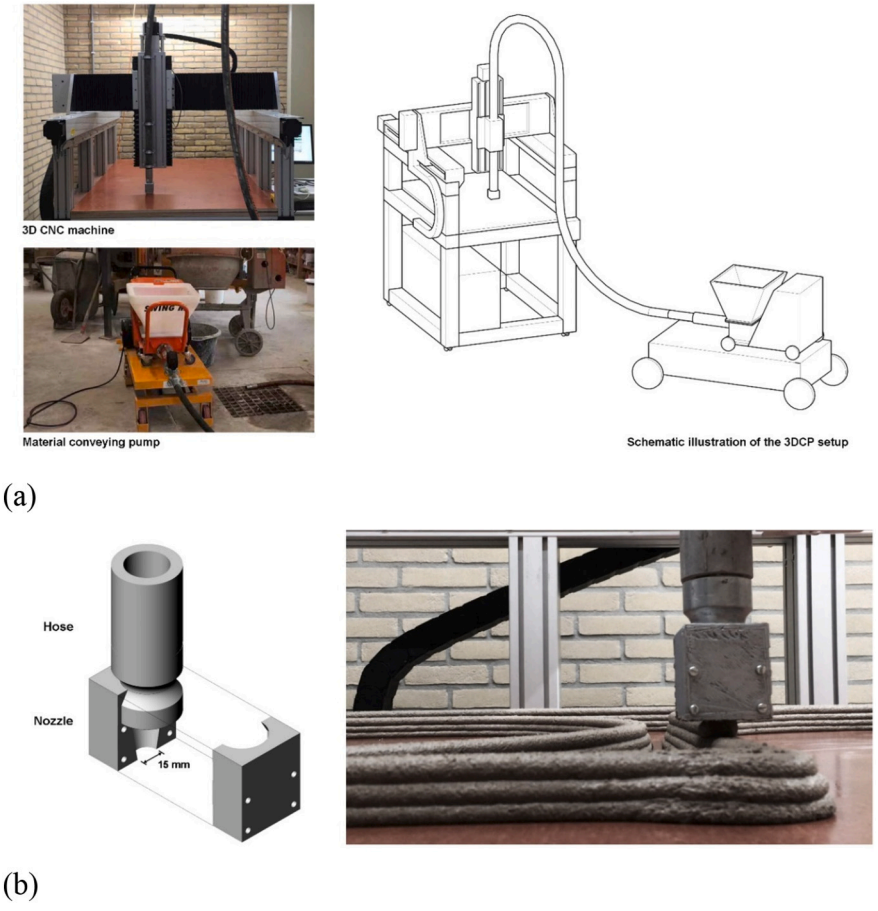

Fig. 3. A lab-scale 3DCP configuration at TU Delft: (a) 3D CNC table and material conveying pump; (b) Down-flow nozzle with a round opening (Ø 15 mm), adapted from [7].

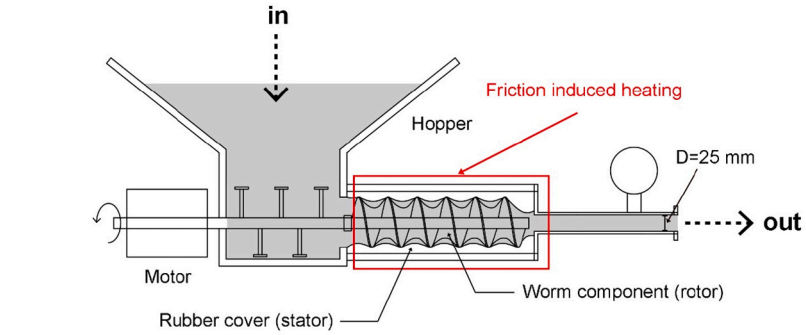

(a)

(b)

Fig. 4. (a) Illustration of the section of material conveying pump; (b) Measurements of material flow rate and increased temperature ($T = T_2$-T_1).

where A is the area of nozzle opening (mm^2). Due to the time-dependent properties of cementitious materials, the workability of fresh mixture should change with time. Besides, the fresh mixture may suffer high friction when it passes through the rotor-stator component, which appears to increase the material temperature. Such effects could also accelerate the workability loss of fresh cementitious material. The change of material rheology (in terms of workability loss) can lead to a decrease in material flow rate during printing, which severely affects the printing quality. For example, when $V_n > Q_{linear}$, the extruded filaments become thinner or even discontinuous (see [4,34,38]). Thus, in this study, we proposed an extrudability window test, which was based on the pumpability test by [31] and open time test by [4,11,16], to characterize the change of material flow rate with time. The test procedures were summarized as follows:

- First, about 8 L of the fresh mixture was prepared in accordance with the mixing protocol in Table 3. The freshly mixed material was poured in the hopper of the material conveying pump and the surface temperature of fresh mixture T_1 was measured by using a non-contact thermometer (TENMA) (see Fig. 4 (b)).
- Second, the extrusion test was started at the material age of 15 min (the time since water addition). Note that the material hose was not used since the tested material may lead to blockage during testing. Under a constant pumping rate of 58–60 rpm, the fresh mixture was delivered through the pump and the surface temperature of the extruded material T_2 was measured as well (see Fig. 4 (b)). The extruded material was collected for about 10 s. The mass of collected material and the unit of weight of the mixture were employed to compute the real-time material flow rate. This process was repeated twice for each mixture. Besides, the extruded material was also used to conduct the setting time test (see Section 2.2.3.1).
- Afterwards, the extrusion trial was repeated at the material age from 30 min to 2 h with a time gap of 10 min. For some mixtures, this test may be terminated earlier if the loss of material flow rate is more than 30%. Concerned about the thixotropy of fresh cementitious materials, a pre-extrusion session was designed at the last 2 min of the time gap. The pump was initiated at a 58–60 rpm pumping rate to extrude fresh cementitious material during the pre-extrusion session. The measurement was not started until the continuous filament was obtained (see Fig. 4 (b)).

We proposed two indicators in this test, i.e., extrudability window and operation window. The former one was defined as the time window for ensuring a good printing quality (the loss of material flow rate is less than 5%). The operation window was the maximum time to perform the printing work using one-batch material (the loss of material flow rate is less than 30%). If exceeding the operation window, the material with high stiffness may block the hose. Note that the hose/pipe (parameters: length, diameter and others) used to transport the cementitious material from the pump to the nozzle can also influence the pumpability and extrudability of the studied cementitious material, especially when the pumping distance is quite long in large-scale concrete printing (see [5,70]). Such effects were not considered since a short hose (5 m) was employed in our current application. In further research, we will study the pumpability of studied mixtures for upscaling printing works.

2.2.2.3. Buildability test. The 3DCP setup, as introduced in Section 2.2.2.1, was employed to perform the buildability test. The test process is illustrated in Fig. 5. A hollow cylinder with a 200 mm diameter was printed by using different mixtures to evaluate their buildability. The nozzle was moved up with a height of 8 mm at the end position of each layer. Thus, the designed layer thickness was about 8 mm, whereas this thickness may be increased with the increase of nozzle standoff distance

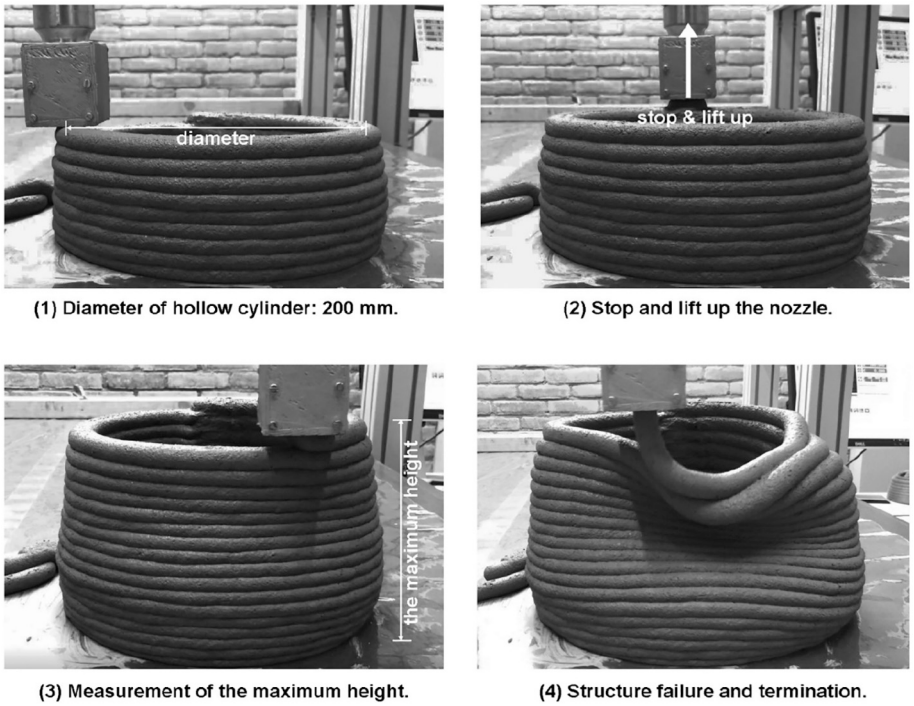

Fig. 5. Example of the buildability test process.

induced by the deformation of the bottom layers. The pumping rate of 58–60 rpm (the same as the speed in the extrudability window test) was kept identical for various mixtures. Within the extrudability window, the material flow rate of one fresh mixture could be a relatively constant value, which was used to compute the nozzle moving speed using Eq. (2). Therefore, the test time should not exceed the extrudability window of the fresh mixture. According to studies [7,11,31], the maximum number and height of deposited layers before collapsing were recorded as indicators for this test.

2.2.3. Characterization of stiffness development and early-age hydration

2.2.3.1. Stiffness evolution with time. The initial setting time of studied mixtures was measured via an automatic Vicat test apparatus. The test was performed under NEN-EN 196-3 [71]. Both regular cast (directly use the material after mixing) and "pump" cast (extruded material from Section 2.2.2.2) mortars were tested in this study. In addition to measuring initial setting time, the plate stacking test (see [14,23,59,72,73]) was used to evaluate the shape stability of different mixtures at 15 min, 30 min, 1 h and 2 h, which can also indicate the evolution of green strength (or stiffness). Cylindrical molds (internal diameter: 60 mm; height: 35 mm) were employed to cast fresh samples. Plates (static load) were gradually placed on top of the demolded sample one by one. The sample's height was recorded after being added to the static load. Under the same static load, the higher the sample's height, the higher the shape stability of the mixture.

From a microstructural point of view, the evolution of material stiffness seems to be dominated by the nucleation and growth of hydrates between particles [74], resulting in a considerable increase of SSA_{total} [75]. Therefore, SSA_{total} of each studied mixture (paste) was measured at the material ages of 1 h and 3 h in this paper. Solvent exchange with isopropanol was employed to stop the hydration of paste samples (details can be found in [7,75,76]). For determining the total SSA (SSA_{total}) of hydrated cementitious materials, dry powders (after the hydration process was stopped) were gently homogenized in an agate mortar. By using a BET multi-point nitrogen (N_2) physisorption apparatus (Gemini VII 2390), the SSA_{total} of dry powders was measured.

2.2.3.2. Isothermal calorimetry and compressive strength tests. For the isothermal calorimetry test, an eight-channel TAM Air isothermal calorimeter was employed to determine the reaction heat induced by cement hydration during the first 7 days. The test process was the same as described by [4,7]. Fresh pastes were prepared by following the mixing protocol in Table 3. For each mixture, 5 g of freshly prepared paste was filled in a 20 mL glass vessel. Afterwards, the sealed vessel was placed in the calorimeter under 20 °C. Heat values were recorded each 20 s for 7 days (168 h). Mold-cast mortar specimens (40 mm cube) were prepared and tested at the material ages of 1, 3, 7, and 28 days to monitor the evolution of compressive strength with time. All specimens were cured and stored in a fog room (20 ± 2 °C, and above 95% RH) until conducting the test. According to NEN-EN 196-1 [77], a loading rate of 2.4 kN/s was employed to perform the compressive strength test. For each mixture at each material age, the average value of compressive strength was obtained through 3 repeated tests.

3. Results

3.1. Mix designs and fresh properties

3.1.1. Slump and slump-flow

According to the preliminary test, W/B of 0.3 could not maintain mixtures in Table 2 saturated without adding SP. Thus, 0.5–2% (of the binder mass) of SP with a 0.5% increment was added into mixtures. The slump and slump-flow test results of these mixtures containing a certain amount of SP are illustrated in Fig. 6. Mixtures with relatively weak flowability exhibited a considerable height after demolding (Fig. 6 (a)), and a small spread diameter after the table dropped 25 times (Fig. 6 (b)). It could be found that 0.5% SP only satisfied the demand of mixture B0. For mixtures B45, B75 and B90, the required minimum dosage of SP was increased with the increase of CC and LF content. The high PCE-based SP demand for calcined clay/MK-based cementitious materials has been reported by [62,65,78,79]. This may be mainly induced by the high SSA and layered particle structure of calcined clay if the swelling clay, e.g., montmorillonite, was not available. Overall, at least 1.5% SP was required to keep all mixtures saturated, and the addition of 2% SP

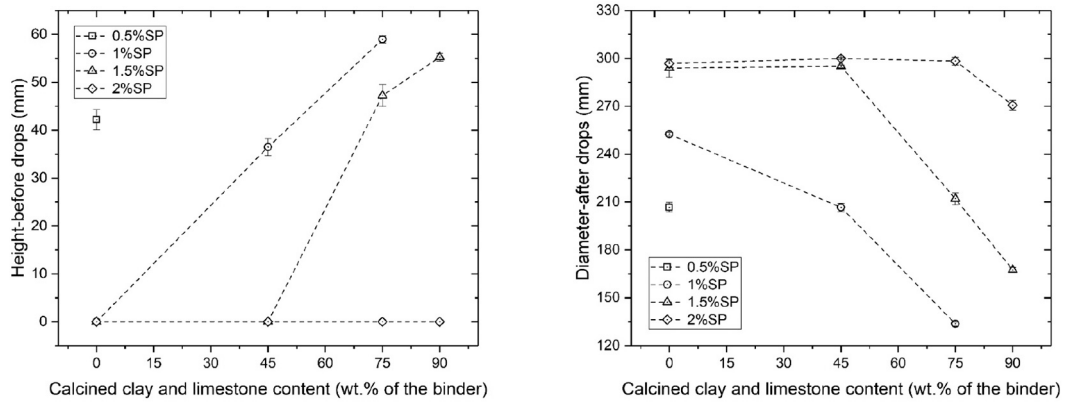

(a) (b)

Fig. 6. Slump and slump-flow test results of mixtures with different SP dosages: (a) Height (before table drops), the height smaller than 20 mm is recorded as 0 mm; (b) Spread diameter (after 25 times of table drops).

resulted in the similar flowability of all fresh mixtures.

For modifying rheology and enhancing water retention property of studied mixtures, 0.12–0.36% (of the binder mass) of VMA was mixed in the fresh mixtures with 1.5% of SP. As shown in Fig. 7, increasing the dosage of VMA can reduce the slump of demolded sample and the spread diameter. Also, the increase of CC and LF content can improve the shape retention capacity and reduce the flowability of tested samples. Almost zero-slump can be found in Fig. 7 (a) for mixtures B75 and B90 with the addition of 1.5% SP and 0.36% VMA. As reported by Chen et al. [4], the fresh mixtures with a spread diameter above 140 mm may give a good extrudability. Besides, the high dosage of VMA could lead to excessively high pumping pressure (which limits the material flow rate), high porosity of the printed filament and adverse effects on hydration. Thus, 0.36% of VMA was not considered for further tests in this paper. The mixtures with 0.24% VMA showed a much smaller slump value and moderate spread diameter compared to that of mixtures containing 0.12% VMA. If the addition of 0.24% VMA was kept identical, increasing SP dosage from 1.5% to 2% in mixtures B75 and B90 can enhance the flowability and only slightly affect the slump of demolded sample, as shown in Fig. 7.

3.1.2. Water retention capacity

Based on the results of slump and slump-flow tests, three admixture options, i.e., 1.5% SP + 0.12% VMA, 1.5% SP + 0.24% VMA, and 2% SP + 0.24% VMA (only for mixtures B75 and B90) were employed for assessing the water retention property of fresh mixtures. Also, 1.5% SP was designed as a reference. Fig. 8 shows the water retention capacity of different mixtures containing different dosages of SP and VMA. For these mixtures with 1.5% SP, the increase of VMA addition could significantly

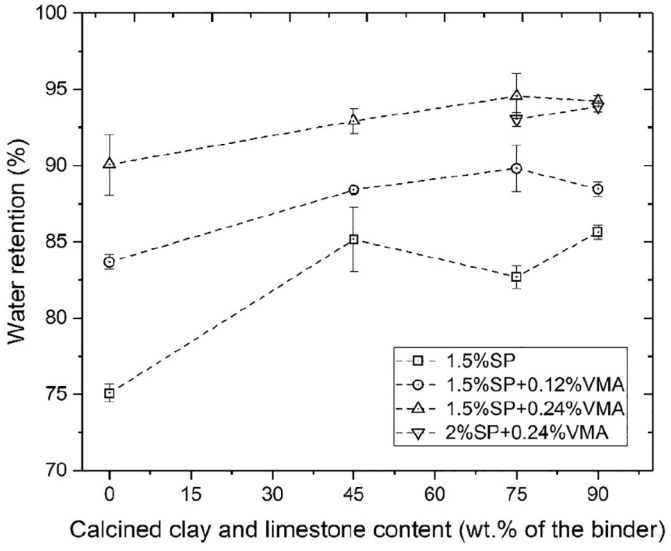

Fig. 8. Water retention of fresh mixtures with different dosages of SP and VMA.

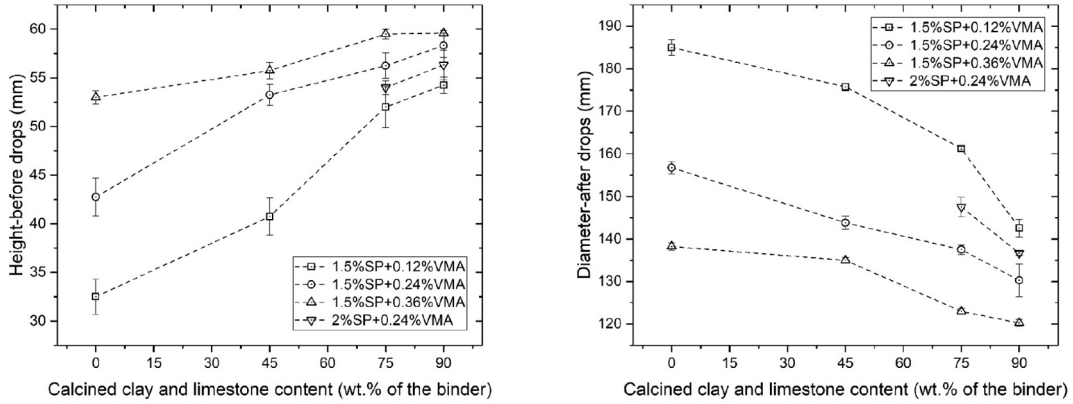

Fig. 7. Slump and slump-flow test results of mixtures with different dosages of SP and VMA: (a) Height (before table drops); (b) Spread diameter (after 25 times of table drops).

improve the water retention property. These results confirmed that the water retention of cellulose ether-derived polymer (HPMC in this paper) primarily depends on the concentration used in the mixture [80]. Besides, as shown in Fig. 8, more quantities of water were retained in mixtures containing LF and CC (B45, B75 and B90) in comparison with mixture B0 for the same admixture addition. This might be attributed to the water adsorption on (calcined) clay minerals. Such water adsorption behaviors of kaolinite, illite and montmorillonite clays have been comprehensively studied by Hatch et al. [81]. Additionally, mixtures with 2% SP + 0.24% VMA showed very close water retention value compared to mixtures with 1.5% SP + 0.24%VMA. The possible reasons why the higher SP content did not result in more amount of bleed water have been explained by Rahul et al. [35]. The high content of SP may lead to many non-adsorbing PCE polymers remained in the suspension, which could increase the viscosity of pore solution [35] and generate a kind of depletion force resulting in particle flocculation [82,83]. Such effects may raise difficulties of bleeding and enhance the water retention capacity of fresh mixtures.

According to results of water retention, slump and slump-flow tests, mixtures including 1.5% SP + 0.24% VMA exhibited good shape retention (small slump after demolding), moderate flowability, and optimal water retention capacity. Thus, 1.5% SP + 0.24% VMA was selected for all mixtures. Acceptable fresh properties could be observed in mixtures B75 and B90 with 2% SP + 0.24% VMA, which were also employed for further characterization. Table 4 presents all mix designs prepared for the following assessments. Note that B0-1 was not used for 3D printing and designed as a reference for determining the effect of increasing CC and LF fractions on the early age hydration.

3.2. Printability

3.2.1. Extrudability and operation windows

Fig. 9 (a) gives the material flow rates of various mixtures at different material ages. Under the same pumping rate of 58–60 rpm, the material flow rate of different mixtures at the same material age was not similar due to the various rheological properties. Under an identical extrusion shearing, mixtures demonstrating a relatively low flow rate may have the high Bingham rheological parameters (yield stress and/or plastic viscosity). At the materials age of 15 min, mixture B90-1 showed the minimum material flow rate. A similar initial material flow rate can be found in mixtures B45-1 and B75-1. Compared to mixtures B75-1 and B90-1, mixtures B75-2 and B90-2 had a much higher material flow rate induced by the 0.5% SP increment. For mixtures B75-1 and B90-1, the loss of material flow rate was evident after 30 min. The change of material flow rate can be attributed to the loss of material workability with time. However, for mixtures B45-1, B75-2 and B90-2, the relatively constant material flow rate can be maintained for a long time. The material flow rate of mixture B45-1 could be kept at about 0.9 L/min during the first 2 h. For the same admixture addition (1.5% SP + 0.24% VMA or 2% SP + 0.24% VMA), increasing the CC and LF content could result in a fast change of material flow rate. Based on the definition of extrudability and operation windows in Section 2.2.2.2, Fig. 9 (b) presents the results of both windows for different mixtures. Mixtures B75-1 and B90-1 exhibited relatively short times for extrusion and operation. In contrast, the increase of 0.5% SP (mixtures B75-2 and B90-2) can extend both extrudability and operation windows about 20–50 min.

The increased material temperatures between before and after extrusion for each mixture at different material ages are plotted in Fig. 9 (c). The mixture with a low material flow rate shows a relatively high temperature increase, as seen from Fig. 9 (d). This is probably induced by the high friction between the mixture and the rotor-stator setup during extrusion. For a constant rotation speed (the shear stress is kept identical), such friction was primarily dominated by the rheological behavior of mixtures at the tested time. Besides, the generated heat could influence the stiffness evolution (initial setting) of deposited materials, which was studied in Section 2.2.3.1.

3.2.2. Buildability

The printing parameters for performing buildability tests are summarized in Table 5. The pump rate was kept at 58–60 rpm that was the same as the one used in the measurement of extrudability and operation windows. According to the test result of extrudability window, all studied mixtures can maintain a relatively stable material flow rate at the material age of 15–30 min. Thus, the buildability test was conducted within this period. The obtained flow rate of different mixtures at the ages of 15–30 min was employed to compute the linear extrusion speed Q_{linear} (see Table 5). As mentioned earlier, to ensure continuous printing, the nozzle moving speed V_n was kept almost equal to the linear extrusion speed of the material Q_{linear}. Due to the different rheological behaviors, the printing speed (nozzle moving speed and material flow rate) of different mixtures was not the same in buildability test. This inequality led to the variation of the time gap between layers. However, owing to the short length of the printing path for each layer used in this test, the time interval deviation between different mixtures was tiny. As seen from Table 5, the maximum difference of time gap is only about 2.3 s. Therefore, the influence caused by the different time gaps on the buildability test was not considered.

The buildability test process and results are presented in Figs. 10 and 11. It could be found that mixture B90-1 exhibited the optimal buildability and can be used to stack more than 20 layers vertically without collapse. The buildability test of mixture B90-1 was terminated at the 21st layer due to the insufficient amount of material in the hopper. As shown in Fig. 11, mixtures B75-1 and B90-2 displayed similar buildability, and the printed structure could reach at most 18 layers. By using mixtures B45-1 and B75-2, only 12 layers were stably deposited. Therefore, with the same addition of admixture (SP + VMA), the mixture containing a higher content of CC and LF can stack more layers and demonstrated a better buildability. Besides, increasing SP dosage from 1.5% to 2% clearly weakened the buildability of fresh mixtures.

As illustrated in Fig. 10, the final buckling collapse (except mixture B90–1) can be attributed to the local or global instability of the printed structure, initiated by large plastic deformations occurring in the bottom layers. The unstable layer deposition was induced by the increase of nozzle standoff distance h_1 that decreased the contact area between layers (see Fig. 12). As reported in our earlier study [7], due to the employment of a down-flow nozzle with a round opening, the new layer was built on the top of the substrate via a squeezed forming process at the beginning of the printing session. This means that the bottom layers should sustain the load not only from the weight of freshly deposited layers but also from the nozzle (when 8 mm $\leq h_1 <$ 15 mm). These forces can lead to the increase of plastic material deformation of the substrate, contributing to the increase of nozzle standoff distance. With increasing

Table 4
Amounts of admixtures for acceptable printing performance of the binders formulating the printable cementitious materials.

	Binder + water + aggregate	Admixture	
	Based on Table 2	Superplasticizer (wt% of the binder mass)	Viscosity modifying admixture (wt% of the binder mass)
B0-1	B0	1.5	0.24
B45-1	B45	1.5	0.24
B75-1	B75	1.5	0.24
B75-2	B75	2.0	0.24
B90-1	B90	1.5	0.24
B90-2	B90	2.0	0.24

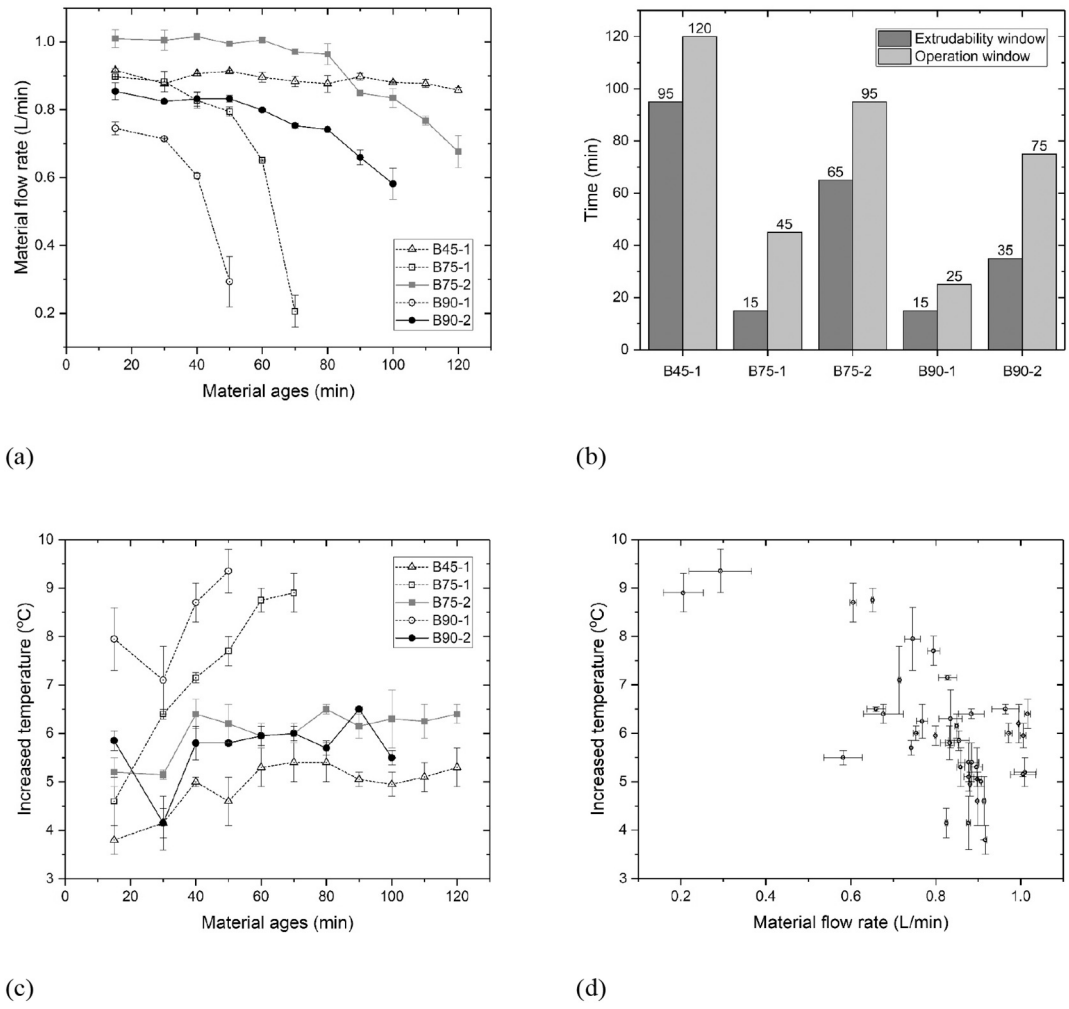

Fig. 9. (a) Material flow rates of different mixtures at various material ages; (b) Test results of extrudability and operation windows; (c) Increased temperatures (after extrusion) of different mixtures at various material ages; (d) Correlation between material flow rates and increased temperatures after extrusion.

Table 5
Printing parameters for performing buildability test.

	Test time (material age) [min]	Predefined nozzle standoff distance [mm]	Pump rate [rpm]	Material flow rate [L/min]	Nozzle opening (diameter) [mm]	Nozzle moving speed [mm/min]	Time gap between layers [s]
B45-1	15–30	8	58–60	0.90	15	5100	7.4
B75-1	15–30	8	58–60	0.89	15	5040	7.6
B75-2	15–30	8	58–60	1.01	15	5700	6.7
B90-1	15–30	8	58–60	0.73	15	4140	9.0
B90-2	15–30	8	58–60	0.85	15	4800	8.1

the nozzle standoff distance, the squeezing force from nozzle was decreased gradually (when 8 mm < h_1 < 15 mm), and then disappeared when the nozzle standoff distance was equal to or larger than the diameter of nozzle opening (when $h_1 \geq 15$ mm). Overall, structure collapse in the buildability test is dominated by the large cumulative plastic deformation of bottom layers. For the mixture with a good buildability, the material deformation during the layer-stacking was not significant. For example, the printed structure manufactured using mixture B90-1 showed relatively even layer thickness from the bottom to the top.

3.2.3. Correlation between inline and offline test results

The test results in this study confirmed that slump and slump-flow tests could indicate the buildability and extrudability/pumpability of 3D printable cementitious materials. A linear relationship between the sample height after demolding in slump test and the maximum height of printed structure before collapsing is illustrated in Fig. 13 (a). Similar findings have been reported elsewhere [31]. The height of demolded sample in the slump test depends on the static yield stress of the tested cementitious material [75,84,85]. As previously described, the buildability of fresh mixtures is dominated by their static yield stress at rest

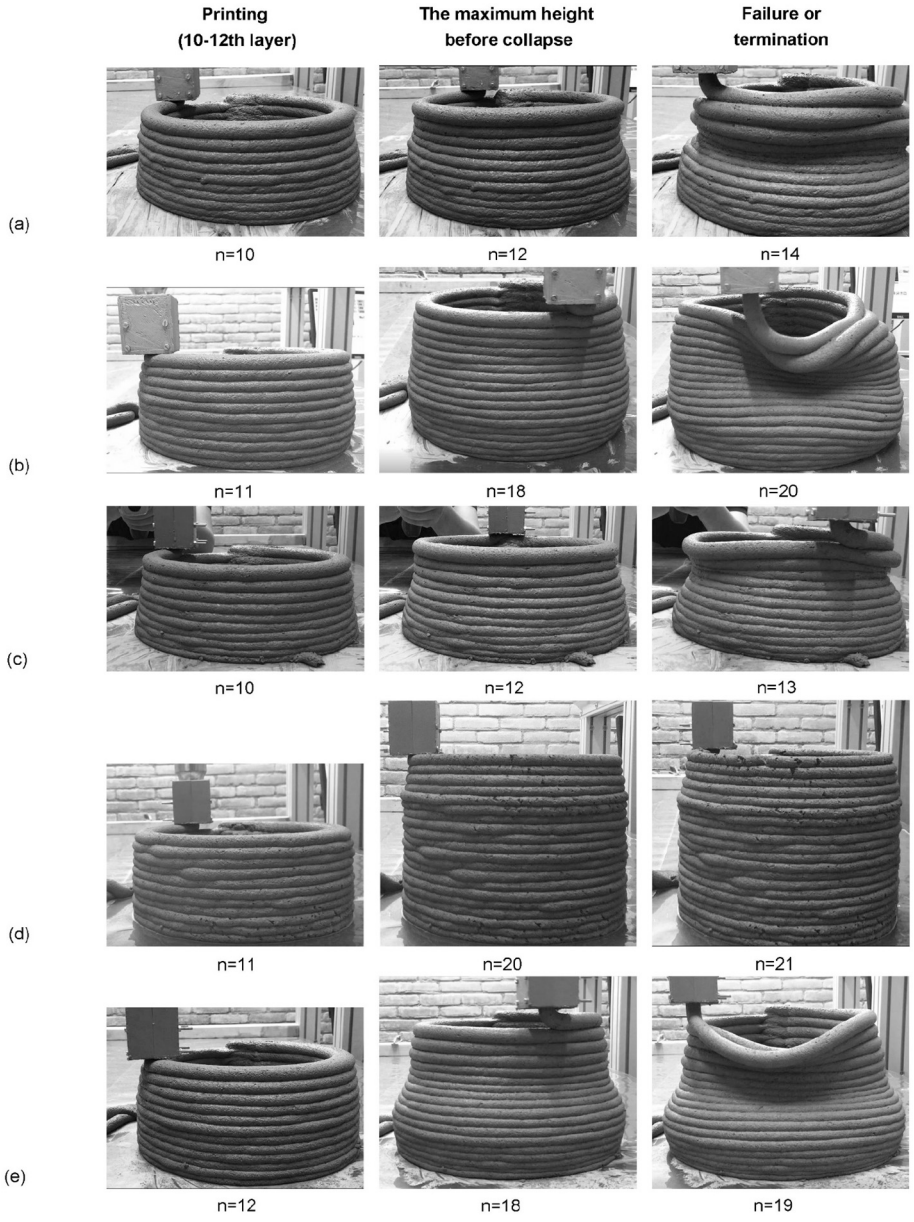

Fig. 10. Buildability tests of mixtures (a) B45-1; (b) B75-1; (c) B75-2; (d) B90-1; (e) B90-2.

[27,29,39] when all printing parameters (e.g., printing speed, nozzle standoff distance, and time interval between layers.) are kept identical. The high static yield stress indicates a good buildability in general. Moreover, as seen from Fig. 13 (b), the spread diameter of different samples after 25 times of table drops in slump-flow test seems linearly correlate with the material flow rate under 58–60 rpm at the similar material age. The mixture with a high spread diameter showed a high flow rate, indicating a high flowability and low dynamic yield stress. Overall, employing slump and slump-flow tests can be employed as a simple and efficient way to formulate printable cementitious materials at an early stage. However, using Hägermann cone is not the conventional way to perform the slump test for mortar. The mold height of Hägermann cone is only 60 mm, which may be insufficient for comparing some mixtures with very high static yield stress (zero-slump after demolding). Generally, it is suggested to use a mini-slump cone with 50 mm top diameter, 100 mm base diameter, and 150 mm height for conducting the slump test of mortar (see [16]).

3.3. Stiffness development and early-age hydration

3.3.1. Stiffness evolution with time

Fig. 14 (a) compares the initial setting time of different mixtures prepared by a regular casting process or by a pump-casting (after extrusion) process. The pump-casting process can accelerate the initial set of the studied mixtures. The reduction of initial setting time for different mixtures was various and ranged between 23 min and 50 min. As reported in Section 3.2.1, the temperature of mixture was increased during extrusion, which accelerated the water loss of fresh mixture. This may explain the acceleration of initial set induced by the pumping process. Besides, increasing the temperature of cementitious materials may enhance the structuration rate at rest, hydration rate of cement, and formation rate of hydration products [86]. Such effects were not studied in this paper and will be investigated in the future.

As shown in Fig. 14 (a), for the same admixture addition, the mixture with a high dosage of CC and LF displayed a short initial setting time. In addition, Fig. 14 (b) illustrates that the shape stability under static load in the first 2 h was enhanced by increasing the amount of LF and CC.

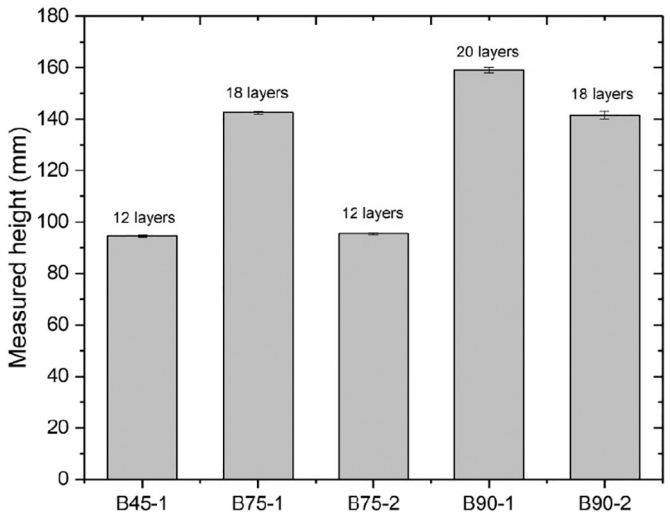

Fig. 11. Buildability test results of different mixtures: the measured maximum height of printed structure before collapse.

However, a slight increase of SP in mixtures (see B90-2 and B75-2) can significantly delay the initial setting, and adversely affect the shape stability and stiffness evolution. These phenomena will be discussed in Section 4.2.

The test results of SSA_{total} at 1 h and 3 h are plotted in Fig. 15 (a). For the same admixture addition, mixtures containing a high dosage of LF and CC showed a great high SSA_{total} at both tested material ages. This was due to the relatively high SSA of CC and the fast growth of SSA_{total} during 1–3 h (see Fig. 15 (b)). By increasing the SP dosage (for mixtures B75 and B90), the evolution of SSA_{total} between 1 h and 3 h was severely decelerated, whereas this influence on SSA_{total} at the first hour was very limited. The increase of SSA_{total} within the first hour was probably attributed to the precipitation of some earlier hydration products (likely ettringite [87], and/or other hydrated aluminate phases) during the initial mixing stage [75]. More discussions about the development of SSA_{total} will be given in Section 4.2.

3.3.2. *Isothermal calorimetry and compressive strength*

Fig. 16 compares isothermal calorimetry test results of different studied paste mixtures. The normalized heat flow and cumulative heat by mass of paste with 7 days are plotted in Fig. 16 (a) and (b), respectively. With the increase of PC substitution by LF and CC, both the intensity of the main hydration peak in Fig. 16 (a) and the cumulative heat

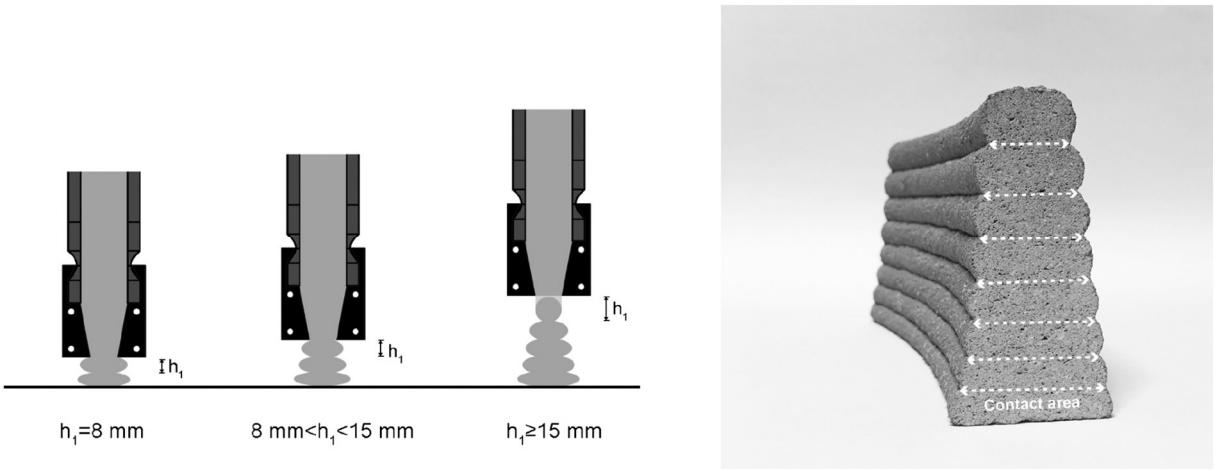

Fig. 12. Illustration of the increased nozzle standoff distances and the expected cross-section of printed structure during printing (left) and a photograph of the cross-section of printed sample using the down-flow nozzle with a round opening (right, adapted from [7]).

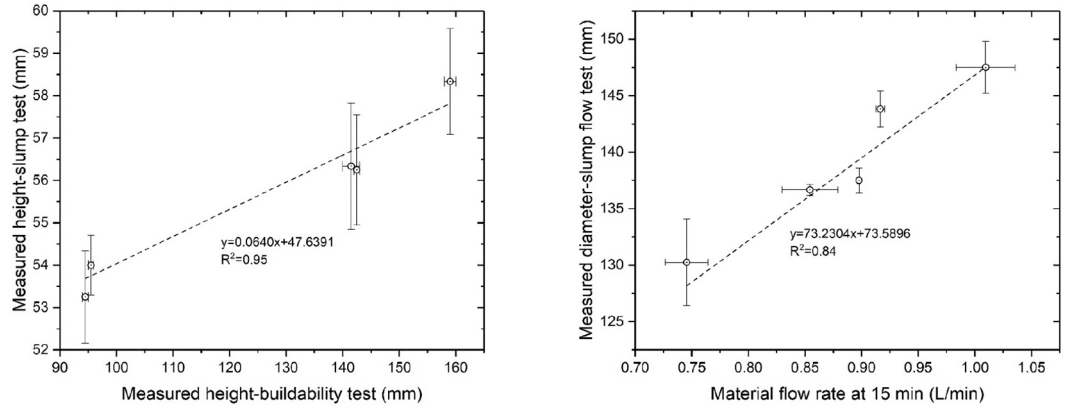

Fig. 13. The linear correlation between (a) Measured sample height in slump test and measured printed structure height in buildability test; (b) Measured spread sample diameter in slump-flow test (after 25 times of table drops) and material flow rate (under 58–60 rpm) at 15 min in extrudability window test.

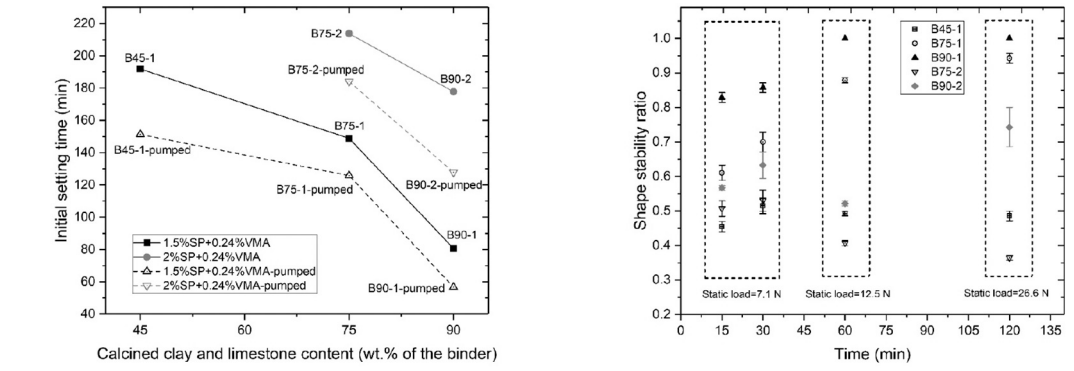

(a) (b)

Fig. 14. (a) Results of the initial setting time; (b) Results of the plate stacking test. Shape stability ratio = Sample height after adding static load/Sample height before adding static load. Static load: 7.1 N (15 min and 30 min), 12.5 N (1 h), and 26.6 N (2 h).

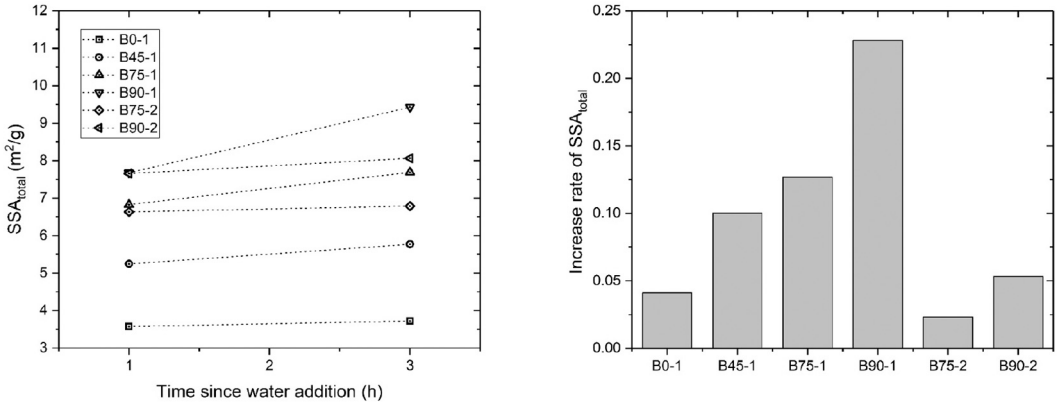

(a) (b)

Fig. 15. (a) SSA_{total} of different paste mixtures at the material ages of 1 h and 3 h; (b) Growth rate of SSA_{total} of different paste mixtures between 1 h and 3 h.

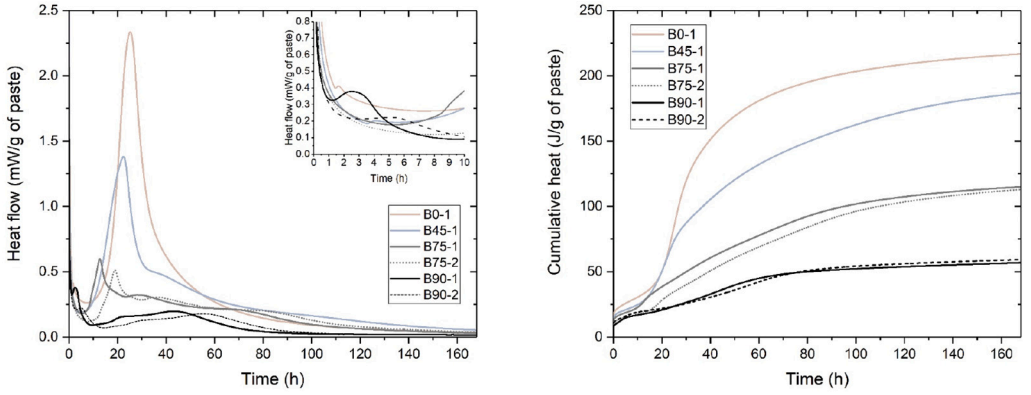

(a) (b)

Fig. 16. Test results of isothermal calorimetry: (a) Normalized heat flow by mass of paste with time (7 days); (b) Normalized cumulative heat by mass of paste with time (7 days).

value at 7 days in Fig. 16 (b) were significantly decreased, which indicated the dilution effect on hydration. Moreover, the retardation of hydration caused by the higher SP dosage can also be observed in Fig. 16. Compared to mixtures B75-1 and B90-1, the main hydration peak of mixtures B75-2 and B90-2 were delayed about 6–8 h. However, such effects only retard the early-age hydration and do not heavily modify the cumulative heat value at 7 days (see Fig. 16 (b)).

The compressive strength test results of different mixtures (mold-cast mortar) at 1, 3, 7 and 28 days are presented in Fig. 17 (a). For the same dosage of SP and VMA, increasing the content of CC and LF in the binder

decreased the compressive strength at all tested ages. Mixture B0-1 containing 0% of CC and LF showed the optimal compressive strength among all mixtures. In comparison with mixture B0-1, mixture B45-1 displayed much lower early-age compressive strength, i.e., 1 and 3 days, and comparable strength at 7 and 28 days, which agreed with the findings of Avet et al. [67]. The moderate compressive strength of about 25 MPa can be obtained at 28 days by replacing 75% of PC with LF and CC (mixtures B75-1 and B75-2). Further reducing the PC content resulted in a significant decrease of compressive strength (mixtures B90-1 and B90-2). Moreover, for mixtures B75 and B90, the increase of SP dosage from 1.5% to 2% can reduce nearly 50% of compressive strength at 1 day, whereas such influences were diminished obviously from 3 days onwards.

If all cast samples with the similar air void content and distribution, the compressive strength may mainly depend on the hydration of cementitious materials. A linear correlation between the compressive strength of mortar and the normalized cumulative heat value of paste at 1, 3 and 7 days is illustrated in Fig. 17 (b). The R-squared value of the fitted curve was higher than 0.9, which appeared to confirm the critical role of cement hydration on the compressive strength of cast samples in this context.

4. Discussion

4.1. Effect of increasing CC and LF content on flowability and 3D printability

If the dosage of admixtures remains unchanged, the main difference between mixtures in this study is the binder composition. Thus, for mixtures B0-1, B45-1, B75-1, and B90-1, the various material behaviors in aspects of flowability and 3D printability appear to be dominated by the CC and LF content. The physical characteristics, including the total SSA, solid fraction, and packing density, may be modified by increasing the proportion of CC and LF in the binder. In cementitious pastes, the initial role of water is to occupy the voids between particles. In most cases, the water content is higher than the required minimum amount for filling all voids. The excess water may form water films on surfaces of particles to ease the friction between solid particles [88]. Earlier studies [61,88–92] showed that the flowability, rheology and strength of fresh cementitious materials are strongly related to the corresponding water film thickness (WFT). According to [61,89], the WFT of paste can be calculated via the following equations:

$$WFT = \frac{\mu_{excess}}{SSA_0} \tag{3}$$

$$SSA_0 = \frac{V_{PC}SSA_{PC}}{\rho_{PC}} + \frac{V_{LF}SSA_{LF}}{\rho_{LF}} + \frac{V_{CC}SSA_{CC}}{\rho_{CC}} \tag{4}$$

where SSA_0 is the total SSA of dry binder (m^2/cm^3); V_{PC}, V_{LF} and V_{CC} denote the volumetric ratio of PC, LF and CC in the binder; SSA_{PC}, SSA_{LF} and SSA_{CC} stand for the measured SSA (m^2/g) of PC, LF and CC. ρ_{PC}, ρ_{LF} and ρ_{CC} denote the density of PC, LF and CC (see Table 1). μ_{excess} is the excess water volume fraction (the excess water volume/the solid volume), which is obtained by:

$$\mu_{excess} = \mu_{total} - \mu_{void} \tag{5}$$

where μ_{total} and μ_{void} denote the water ratio of the paste (total water volume/the solid volume) and void ratio (total void volume/the solid volume), respectively. μ_{void} is quantified by:

$$\mu_{void} = \frac{1-\tau}{\tau} \tag{6}$$

where τ is the packing density of the binder. In this study, the packing density of each binder was measured by using the Puntke test. The test was conducted under the description given by [35,93]. The mixing liquid in the Puntke test comprised water and 5% SP (1.5% of the binder mass). Note that the packing density used in Eq. (6) can also be acquired via the wet packing method [94] or a packing algorithm [61]. Besides, sand and VMA of each mixture (see Tables 2 and 4) were excluded from the calculation of WFT. The packing density, SSA_0 and WFT of studied cementitious systems are illustrated in Fig. 18. The impact of CC and LF addition on packing density is very limited. Only mixture B90 shows a slight decrease in packing density compared to others. In contrast, increasing the content of LF and CC in the binder leads to a vast increase of SSA_0, which is probably due to the extremely high SSA of CC. Consequently, a steep reduction of WFT was expected as the increase of SSA_0. For the tests performed within 30 min after water addition, i.e., slump and slump-flow, buildability, and extrudability window tests (first two trials), the nucleation and structuration between particles should not start yet. Mixtures with a small WFT of paste (high content of CC and LF) displayed a strong shape retention and buildability, as well as a weak flowability and extrudability (see Figs. 7, 9, 11, 19). Without considering about structural build-up, the rheological performance of fresh mortar is primarily dependent on the WFT of paste and cement (binder in this context) to aggregate ratio [92]. In this paper, the binder to aggregate ratio and aggregate gradation were kept constant for all tested mixtures. Thus, the WFT of pastes as an intrinsic indicator combining many physical features of mixture, i.e., water content, packing density and SSA, plays the most critical role in influencing fresh-

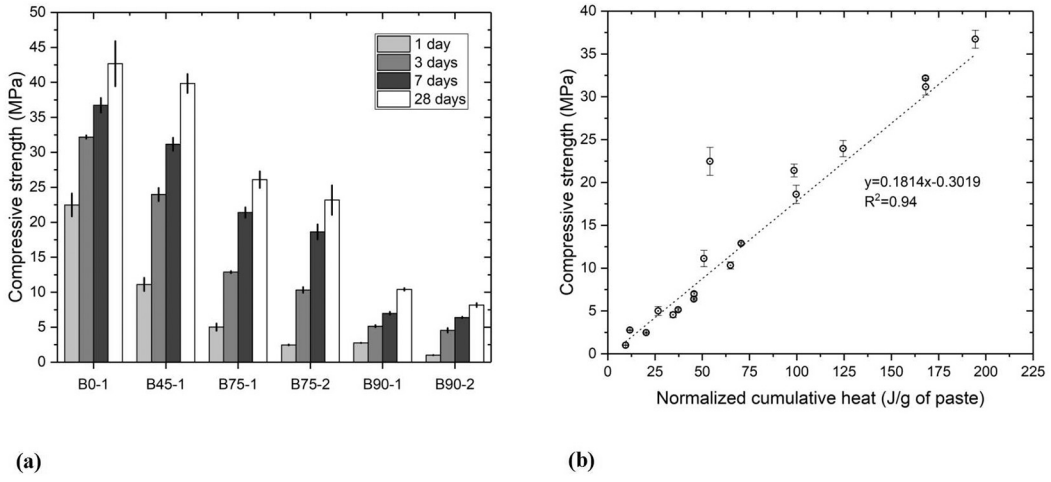

Fig. 17. (a) Compressive strength of different mixtures at 1, 3, 7, and 28 days. (b) The linear relationship between compressive strength and normalized cumulative heat by mass of paste at 1, 3, and 7 days (excluding any heat within the first 2 h after mixing).

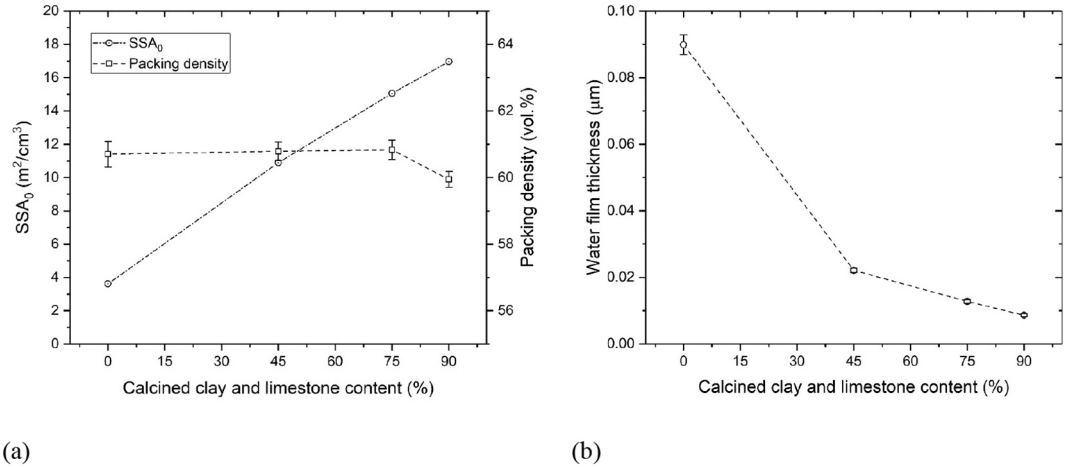

Fig. 18. (a) Packing density and SSA_0; (b) Water film thickness of cementitious systems containing different contents of limestone and calcined clay.

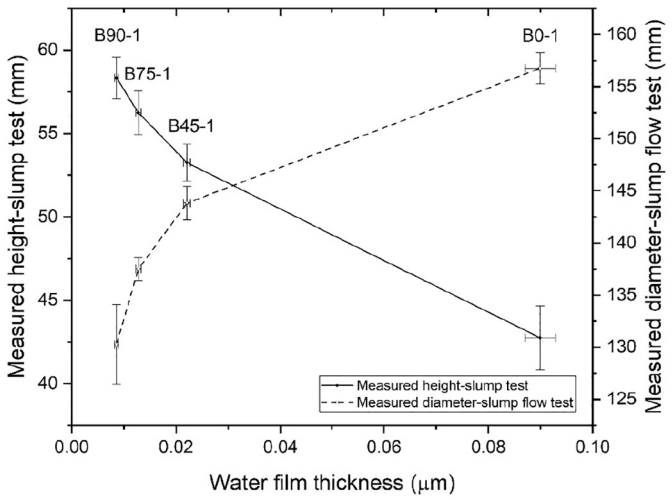

Fig. 19. Correlation between: Water film thickness and measured sample height in slump test; Water film thickness and measured sample diameter in slump flow test.

state behaviors at this stage.

4.2. Effect of increasing CC and LF content on stiffness evolution with time

The structural build-up at rest within the material age of 3–4 h is of great importance for 3D printable cementitious materials considering the printing process. The mixture exhibited a fast stiffness evolution or structuration rate at rest (after deposition) can be regarded as merit in applying 3D printing. For the same addition of admixtures, the results of extrudability test (see Fig. 9) showed that the mixture containing a higher dosage of CC and LF experienced a faster material flowability and extrudability loss (material flow rate). Due to the short gap between two test trials (8 min), the tested materials were not at a constantly dynamic status. The material stiffness appeared to be developed during the short resting time, leading to a gradual workability reduction. Consequently, a significant decrease in material flow rate with time was observed for these mixtures, i.e., mixtures B75-1 and B90-1, which displayed a fast stiffness evolution (see Fig. 14 (b)). Similarly, increasing the LF and CC substitution of the binder accelerates the initial set of fresh mixtures, as shown in Fig. 14 (a).

The LF with the similar fineness and SSA compared to that of PC was used as an ideal inert filler in studied mixtures. In contrast to LF, CC containing a relatively high dosage of reactive aluminate phases (32 wt %) seems to play a dominant role in accelerating the stiffness development of fresh cementitious materials within the first several hours. For the cementitious systems consisted of high content of CC and LF (mixtures B75 and B90), the amount of calcium sulfate (gypsum) was very low due to the limited addition of PC. At the very early age of hydration (3–4 h since water addition), lack of gypsum in the binder system may lead to a sulfate depletion caused by aluminate reaction at the initial stage (see the first peak of mixture B90-1 in Fig. 16), whereas this phenomenon was not observed in mixtures B45-1 and B75-1. Additionally, the formation of massive hydration products (see Fig. A.1), relating to the increase of SSA seems the main reason governing the workability loss and stiffness evolution of fresh mixtures. As shown in Fig. 15, increasing the content of CC and LF in the binder accelerated the development of SSA_{total} during 1–3 h. From the perspective of water film theory in Section 4.1, the increment of SSA_{total} can further reduce WFT affecting the fresh-state behaviors of mixtures (without considering the difference in water consumption).

The stiffness evolution of studied mixtures was also influenced by the presence of PCE-based SP. At the very beginning, PCEs adsorbed on the surface of cementitious particles for dispersing them and controlling their flocculation [75,95]. However, as mentioned by [75], compared to adsorbing on cement particles, PCEs may tend to be consumed by hydrated aluminate phases owing to the preferential sequestration [96,97] or adsorb on ettringite [87,98] at the early-age hydration. The precipitation of such crystal phases can provide more specific surface areas [87], which vastly reduces the available PCEs for the dispersion [75,96,99]. Also, this process could improve the delay of anhydrous phase dissolution caused by PCEs and accelerate the nucleation and hydration of cement [100,101]. For mixtures B75 and B90, the slight increment of SP dosage from 1.5% to 2% can increase the available PCEs in the solid suspension for extending its dispersion effect. The extrudability window of fresh mixture was prolonged due to this effect (see Fig. 9). Nonetheless, the development of material stiffness, as indicated by the initial setting time, shape stability under static load in the first 2 h and the growth rate of SSA_{total} (see Figs. 14 and 15), were severely declined.

5. Conclusion

The objective of the current study is to investigate the effect of replacing a high content of Portland cement (>60 wt%) with a blend of calcined clay and limestone on flowability, 3D printability, stiffness evolution and early-age hydration. Based on the present study, the following conclusions were drawn:

- Increasing the content of LF and CC can decrease both slump and flowability. The obtained results of slump and slump-flow tests were feasible for obtaining the extrudability and buildability of studied mixtures. Increasing VMA% can enhance the shape retention property and water retention capacity of fresh mixtures but affect the corresponding flowability.
- By adding the same admixtures (1.5% SP + 0.24% VMA), the mixtures containing a high content of CC and LF displayed a low material flow rate at the same tested time, short extrudability and operation windows, and a strong buildability. Such effects can be attributed to the reduced WFT of pastes owing to the high SSA of CC.
- The mixture with a low material flow rate displayed a relatively high temperature increase after extrusion. The increase of material temperature induced by the extrusion process can accelerate the water loss of fresh mixture, consequently reducing the initial setting time.
- By increasing the amount of CC and LF in the binder with the same admixture addition, the initial setting and the stiffness evolution were accelerated, and the SSA_{total} was increased at 1 h and 3 h. The SSA_{total} evolution may lead to the reduction of WFT and available PCEs for the dispersion, which appears to govern the stiffness development.
- The dilution effect on hydration and compressive strength was enhanced by the increase of LF and CC content. Due to the weak compressive strength, mixtures containing more than 75% of LF and CC in the binder may not be suitable to be employed as building materials.
- The 0.5% SP increment (see Mixtures B75-2 and B90-2) led to the increase of material flow rate, extrudability and operation windows, initial setting time, the time to the main hydration peak, as well as the reduction of buildability and SSA_{total} at 3 h.

Author statement

The content of this article is new and has not be published or submitted for publication elsewhere.

Declaration of competing interest

All authors have no conflict of interest regarding the content of the research as written in the submitted article.

Acknowledgments

This work is a part of Yu Chen's PhD research. Yu Chen, Zhi Wan and Yu Zhang want to acknowledge the funding supported by China Scholarship Council under grant No. 201807720005, 201906220205, 201808320456.

Appendix A

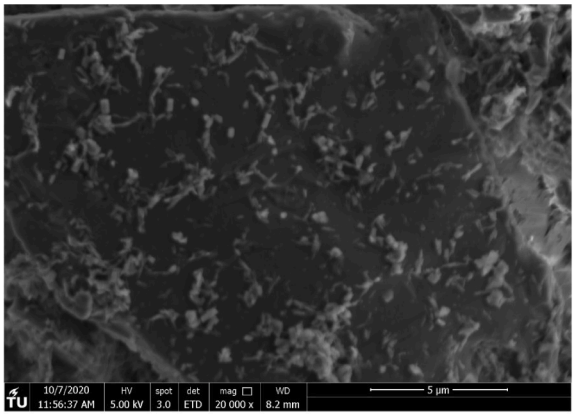
10/7/2020
11:56:37 AM
HV
5.00 kV
spot
3.0
det
ETD
mag
20 000 x
WD
8.2 mm
5 µm

(a)

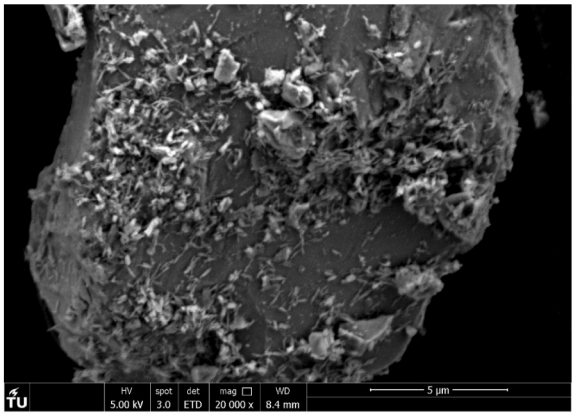
HV
5.00 kV
spot
3.0
det
ETD
mag
20 000 x
WD
8.4 mm
5 µm

(b)

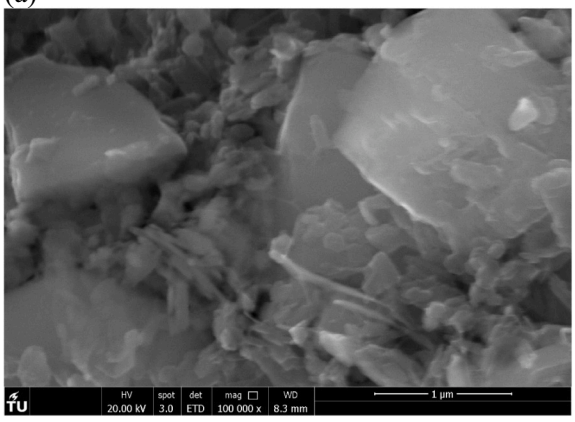
HV
20.00 kV
spot
3.0
det
ETD
mag
100 000 x
WD
8.3 mm
1 µm

(c)

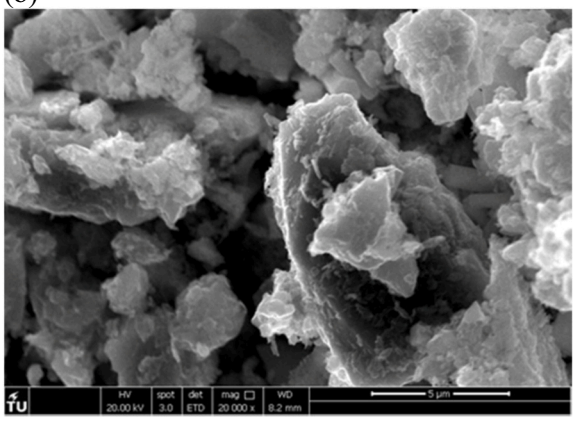
HV
20.00 kV
spot
3.0
det
ETD
mag
20 000 x
WD
8.2 mm
5 µm

(d)

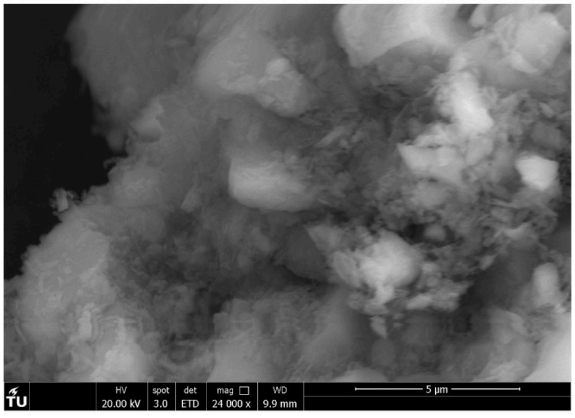
HV
20.00 kV
spot
3.0
det
ETD
mag
24 000 x
WD
9.9 mm
5 µm

(e)

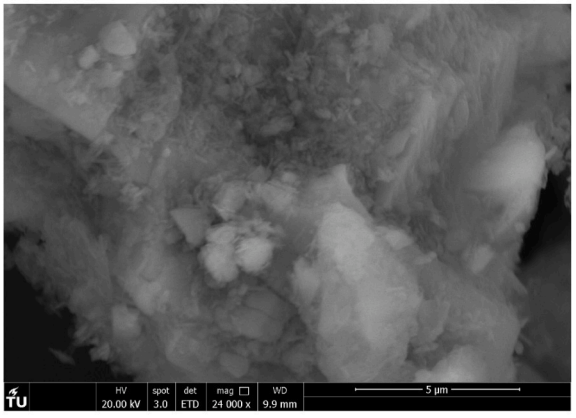
HV
20.00 kV
spot
3.0
det
ETD
mag
24 000 x
WD
9.9 mm
5 µm

(f)

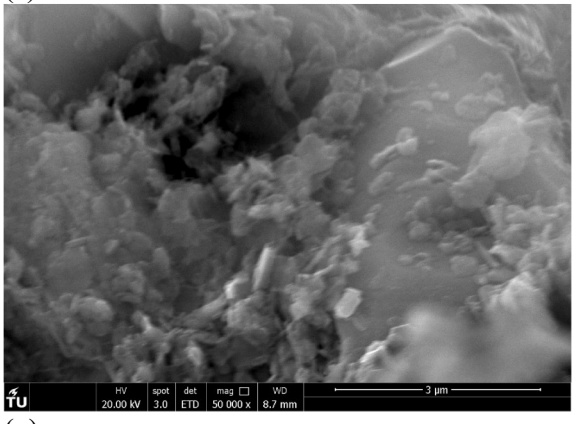
HV
20.00 kV
spot
3.0
det
ETD
mag
50 000 x
WD
8.7 mm
3 µm

(g)

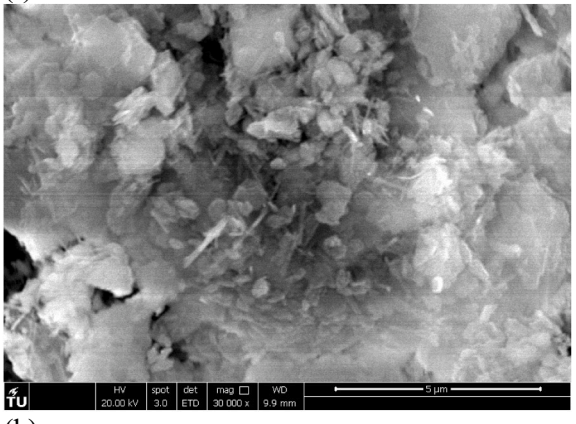
HV
20.00 kV
spot
3.0
det
ETD
mag
30 000 x
WD
9.9 mm
5 µm

(h)

Fig. A.1. Microstructural observation (secondary electron mode)-morphology of hydration products on the surfaces of different particles: (a) B0-1 at 1 h, magnification of ×20,000; (b) B0-1 at 3 h, magnification of ×20,000; (c) B45-1 at 1 h, magnification of ×100,000; (d) B45-1 at 3 h, magnification of ×20,000; (e) B75-1 at 1 h, magnification of ×24,000; (f) B75-1 at 3 h, magnification of ×24,000; (g) B90-1 at 1 h, magnification of ×50,000; (h) B90-1 at 3 h, magnification of ×30,000.

References

[1] G. De Schutter, K. Lesage, V. Mechtcherine, V.N. Nerella, G. Habert, I. Agusti-Juan, Vision of 3D printing with concrete — technical, economic and environmental potentials, Cem. Concr. Res. (2018), https://doi.org/10.1016/j.cemconres.2018.06.001.

[2] R.A. Buswell, W.R. Leal de Silva, S.Z. Jones, J. Dirrenberger, 3D printing using concrete extrusion: a roadmap for research, Cem. Concr. Res. 112 (2018) 37–49, https://doi.org/10.1016/j.cemconres.2018.05.006.

[3] Y. Chen, K. Jansen, H. Zhang, C. Romero Rodriguez, Y. Gan, O. Çopuroğlu, E. Schlangen, Effect of printing parameters on interlayer bond strength of 3D printed limestone-calcined clay-based cementitious materials: an experimental and numerical study, Constr. Build. Mater. 262 (2020), 120094, https://doi.org/10.1016/j.conbuildmat.2020.120094.

[4] Y. Chen, S. Chaves Figueiredo, Z. Li, Z. Chang, K. Jansen, O. Çopuroğlu, E. Schlangen, Improving printability of limestone-calcined clay-based cementitious materials by using viscosity-modifying admixture, Cem. Concr. Res. 132 (2020), 106040, https://doi.org/10.1016/j.cemconres.2020.106040.

[5] V. Mechtcherine, F.P. Bos, A. Perrot, W.R.L. da Silva, V.N. Nerella, S. Fataei, R.J. M. Wolfs, M. Sonebi, N. Roussel, Extrusion-based additive manufacturing with cement-based materials – production steps, processes, and their underlying physics: a review, Cem. Concr. Res. 132 (2020), 106037, https://doi.org/10.1016/j.cemconres.2020.106037.

[6] M.K. Mohan, A.V. Rahul, K. Van Tittelboom, G. De Schutter, Rheological and pumping behaviour of 3D printable cementitious materials with varying aggregate content, Cem. Concr. Res. 139 (2021), 106258, https://doi.org/10.1016/j.cemconres.2020.106258.

[7] Y. Chen, C.R. Rodriguez, Z. Li, B. Chen, O. Çopuroğlu, E. Schlangen, Effect of different grade levels of calcined clays on fresh and hardened properties of ternary-blended cementitious materials for 3D printing, Cem. Concr. Compos. 114 (2020), 103708, https://doi.org/10.1016/j.cemconcomp.2020.103708.

[8] V.N. Nerella, M. Krause, V. Mechtcherine, Direct printing test for buildability of 3D-printable concrete considering economic viability, Autom. Constr. 109 (2020), 102986, https://doi.org/10.1016/j.autcon.2019.102986.

[9] V.N. Nerella, V. Mechtcherine, Studying the printability of fresh concrete for formwork-free concrete onsite 3D printing technology (CONPrint3D), in: 3D Concr. Print. Technol, Elsevier Inc., 2019, pp. 333–347, https://doi.org/10.1016/b978-0-12-815481-6.00016-6.

[10] E. Hosseini, M. Zakertabrizi, A.H. Korayem, G. Xu, A novel method to enhance the interlayer bonding of 3D printing concrete: an experimental and computational investigation, Cem. Concr. Compos. 99 (2019) 112–119, https://doi.org/10.1016/j.cemconcomp.2019.03.008.

[11] T.T. Le, S.A. Austin, S. Lim, R.A. Buswell, A.G.F. Gibb, T. Thorpe, Mix design and fresh properties for high-performance printing concrete, Mater. Struct. Constr. 45 (2012) 1221–1232, https://doi.org/10.1617/s11527-012-9828-z.

[12] S. Lim, R.A. Buswell, T.T. Le, S.A. Austin, A.G.F. Gibb, T. Thorpe, Developments in construction-scale additive manufacturing processes, Autom. Constr. 21 (2012) 262–268, https://doi.org/10.1016/j.autcon.2011.06.010.

[13] T. Wangler, N. Roussel, F.P. Bos, T.A.M. Salet, R.J. Flatt, Digital concrete: a review, Cem. Concr. Res. 123 (2019), https://doi.org/10.1016/j.cemconres.2019.105780.

[14] A. Kazemian, X. Yuan, E. Cochran, B. Khoshnevis, Cementitious materials for construction-scale 3D printing: laboratory testing of fresh printing mixture, Constr. Build. Mater. 145 (2017) 639–647, https://doi.org/10.1016/j.conbuildmat.2017.04.015.

[15] T. Wangler, E. Lloret, L. Reiter, N. Hack, F. Gramazio, M. Kohler, M. Bernhard, B. Dillenburger, J. Buchli, N. Roussel, R. Flatt, Digital concrete: opportunities and challenges, RILEM Tech. Lett. 1 (2016) 67, https://doi.org/10.21809/rilemtechlett.2016.16.

[16] G. Ma, Z. Li, L. Wang, Printable properties of cementitious material containing copper tailings for extrusion based 3D printing, Constr. Build. Mater. 162 (2018) 613–627, https://doi.org/10.1016/j.conbuildmat.2017.12.051.

[17] A.V. Rahul, M. Santhanam, H. Meena, Z. Ghani, 3D printable concrete: mixture design and test methods, Cem. Concr. Compos. 97 (2019) 13–23, https://doi.org/10.1016/j.cemconcomp.2018.12.014.

[18] Y. Chen, S. Chaves Figueiredo, Ç. Yalçinkaya, O. Çopuroğlu, F. Veer, E. Schlangen, The effect of viscosity-modifying admixture on the extrudability of limestone and calcined clay-based cementitious material for extrusion-based 3D concrete printing, Materials (Basel) 12 (2019) 1374, https://doi.org/10.3390/ma12091374.

[19] S. Chaves Figueiredo, C. Romero Rodríguez, Z.Y. Ahmed, D.H. Bos, Y. Xu, T. M. Salet, O. Çopuroğlu, E. Schlangen, F.P. Bos, An approach to develop printable strain hardening cementitious composites, Mater. Des. 169 (2019), 107651, https://doi.org/10.1016/j.matdes.2019.107651.

[20] S. Chaves Figueiredo, O. Çopuroğlu, E. Schlangen, Effect of viscosity modifier admixture on Portland cement paste hydration and microstructure, Constr. Build. Mater. 212 (2019) 818–840, https://doi.org/10.1016/j.conbuildmat.2019.04.020.

[21] S.A.O. Nair, H. Alghamdi, A. Arora, I. Mehdipour, G. Sant, N. Neithalath, Linking fresh paste microstructure, rheology and extrusion characteristics of cementitious binders for 3D printing, J. Am. Ceram. Soc. 102 (2019) 3951–3964, https://doi.org/10.1111/jace.16305.

[22] N. Roussel, G. Ovarlez, S. Garrault, C. Brumaud, The origins of thixotropy of fresh cement pastes, Cem. Concr. Res. 42 (2012) 148–157, https://doi.org/10.1016/j.cemconres.2011.09.004.

[23] B. Panda, S.C. Paul, L.J. Hui, Y.W.D. Tay, M.J. Tan, Additive manufacturing of geopolymer for sustainable built environment, J. Clean. Prod. 167 (2017) 281–288, https://doi.org/10.1016/j.jclepro.2017.08.165.

[24] B. Panda, M.J. Tan, Experimental study on mix proportion and fresh properties of fly ash based geopolymer for 3D concrete printing, Ceram. Int. 44 (2018) 10258–10265, https://doi.org/10.1016/j.ceramint.2018.03.031.

[25] S.C. Paul, Y.W.D. Tay, B. Panda, M.J. Tan, Fresh and hardened properties of 3D printable cementitious materials for building and construction, Arch. Civ. Mech. Eng. 18 (2018) 311–319, https://doi.org/10.1016/j.acme.2017.02.008.

[26] Y. Weng, Development and Optimization of 3D Printable Cementitious Composites for Printing Applications, Nanyang Technological University, 2019.

[27] Y. Weng, M. Li, M.J. Tan, S. Qian, Design 3D printing cementitious materials via Fuller Thompson theory and Marson-Percy model, Constr. Build. Mater. 163 (2018) 600–610, https://doi.org/10.1016/j.conbuildmat.2017.12.112.

[28] Y. Zhang, Y. Zhang, G. Liu, Y. Yang, M. Wu, B. Pang, Fresh properties of a novel 3D printing concrete ink, Constr. Build. Mater. 174 (2018) 263–271, https://doi.org/10.1016/j.conbuildmat.2018.04.115.

[29] M. Chen, L. Yang, Y. Zheng, Y. Huang, L. Li, P. Zhao, S. Wang, L. Lu, X. Cheng, Yield stress and thixotropy control of 3D-printed calcium sulfoaluminate cement composites with metakaolin related to structural build-up, Constr. Build. Mater. 252 (2020), 119090, https://doi.org/10.1016/j.conbuildmat.2020.119090.

[30] M. Chen, B. Liu, L. Li, L. Cao, Y. Huang, S. Wang, P. Zhao, L. Lu, X. Cheng, Rheological parameters, thixotropy and creep of 3D-printed calcium sulfoaluminate cement composites modified by bentonite, Compos. Part B Eng. 186 (2020), 107821, https://doi.org/10.1016/j.compositesb.2020.107821.

[31] Y.W.D. Tay, Y. Qian, M.J. Tan, Printability region for 3D concrete printing using slump and slump flow test, Compos. Part B Eng. 174 (2019), 106968, https://doi.org/10.1016/j.compositesb.2019.106968.

[32] Y. Chen, S. He, Y. Gan, O. Copuroglu, F. Veer, E. Schlangen, A review of printing strategies, sustainable cementitious materials and characterization methods in the context of extrusion-based 3D concrete printing, Submitted. (n.d.).

[33] Y.W.D. Tay, G.H.A. Ting, Y. Qian, B. Panda, L. He, M.J. Tan, Time gap effect on bond strength of 3D-printed concrete, Virtual Phys. Prototyp. 14 (2019) 104–113, https://doi.org/10.1080/17452759.2018.1500420.

[34] Y.W.D. Tay, M.Y. Li, M.J. Tan, Effect of printing parameters in 3D concrete printing: printing region and support structures, J. Mater. Process. Technol. 271 (2019) 261–270, https://doi.org/10.1016/j.jmatprotec.2019.04.007.

[35] A.V. Rahul, A. Sharma, M. Santhanam, A desorptivity-based approach for the assessment of phase separation during extrusion of cementitious materials, Cem. Concr. Compos. 108 (2020), 103546, https://doi.org/10.1016/j.cemconcomp.2020.103546.

[36] B. Panda, M.J. Tan, Rheological behavior of high volume fly ash mixtures containing micro silica for digital construction application, Mater. Lett. 237 (2019) 348–351, https://doi.org/10.1016/j.matlet.2018.11.131.

[37] B. Panda, M.J. Tan, Material properties of 3D printable high-volume slag cement, in: First Int. Conf. 3D Constr. Print. Conjunction With 6th Int. Conf. Innov. Prod. Constr. (IPC 2018), 2018.

[38] V.N. Nerella, M. Näther, A. Iqbal, M. Butler, V. Mechtcherine, Inline quantification of extrudability of cementitious materials for digital construction, Cem. Concr. Compos. 95 (2019) 260–270, https://doi.org/10.1016/j.cemconcomp.2018.09.015.

[39] B. Panda, S. Ruan, C. Unluer, M.J. Tan, Improving the 3D printability of high volume fly ash mixtures via the use of nano attapulgite clay, Compos. Part B Eng. 165 (2019) 75–83, https://doi.org/10.1016/j.compositesb.2018.11.109.

[40] B. Panda, J.H. Lim, M.J. Tan, Mechanical properties and deformation behaviour of early age concrete in the context of digital construction, Compos. Part B Eng. 165 (2019) 563–571, https://doi.org/10.1016/j.compositesb.2019.02.040.

[41] B. Panda, N.A.N. Mohamed, S.C. Paul, G.V.P.B. Singh, M.J. Tan, B. Šavija, The effect of material fresh properties and process parameters on buildability and interlayer adhesion of 3D printed concrete, Materials (Basel) 12 (2019) 2149, https://doi.org/10.3390/ma12132149.

[42] K. Mehta, P.J.M. Monteiro, Concrete: Microstructure, Properties, and Materials, 3rd ed., McGraw-Hill, New York, 2006 https://doi.org/10.1036/0071462899.

[43] C. Zhang, Z. Hou, C. Chen, Y. Zhang, V. Mechtcherine, Z. Sun, Design of 3D printable concrete based on the relationship between flowability of cement paste and optimum aggregate content, Cem. Concr. Compos. 104 (2019), 103406, https://doi.org/10.1016/j.cemconcomp.2019.103406.

[44] Y. Chen, F. Veer, O. Copuroglu, A critical review of 3D concrete printing as a low CO_2 concrete approach, Heron. 62 (2017) 167.

[45] Y. Chen, F. Veer, O. Copuroglu, E. Schlangen, Feasibility of using low CO_2 concrete alternatives in extrusion-based 3D concrete printing, in: R. Flatt, T. Wangler (Eds.), RILEM Int. Conf. Concr. Digit. Fabr., Zurich, 2018, pp. 269–276.

[46] M. Mohan, A.V. Rahul, G. De Schutter, K. Van Tittelboom, Early age hydration, rheology and pumping characteristics of CSA cement-based 3D printable concrete, Constr. Build. Mater. 275 (2021) 3, https://doi.org/10.1016/j.conbuildmat.2020.122136.
[47] K. Scrivener, F. Martirena, S. Bishnoi, S. Maity, Calcined clay limestone cements (LC3), Cem. Concr. Res. 114 (2018) 49–56, https://doi.org/10.1016/j.cemconres.2017.08.017.
[48] H. Du, S.D. Pang, High-performance concrete incorporating calcined kaolin clay and limestone as cement substitute, Constr. Build. Mater. 264 (2020), 120152, https://doi.org/10.1016/j.conbuildmat.2020.120152.
[49] M. Antoni, J. Rossen, F. Martirena, K. Scrivener, Cement substitution by a combination of metakaolin and limestone, Cem. Concr. Res. 42 (2012) 1579–1589, https://doi.org/10.1016/j.cemconres.2012.09.006.
[50] W. Huang, H. Kazemi-Kamyab, W. Sun, K. Scrivener, Effect of replacement of silica fume with calcined clay on the hydration and microstructural development of eco-UHPFRC, Mater. Des. 121 (2017) 36–46, https://doi.org/10.1016/j.matdes.2017.02.052.
[51] Y. Dhandapani, T. Sakthivel, M. Santhanam, R. Gettu, R.G. Pillai, Mechanical properties and durability performance of concretes with Limestone Calcined Clay Cement (LC 3), Cem. Concr. Res. 107 (2018) 136–151, https://doi.org/10.1016/j.cemconres.2018.02.005.
[52] K. Scrivener, F. Avet, H. Maraghechi, F. Zunino, J. Ston, W. Hanpongpun, A. Favier, Impacting factors and properties of limestone calcined clay cements (LC 3), Green Mater. 7 (2018) 3–14, https://doi.org/10.1680/jgrma.18.00029.
[53] F. Zunino, K. Scrivener, The reaction between metakaolin and limestone and its effect in porosity refinement and mechanical properties, Cem. Concr. Res. 140 (2021), 106307, https://doi.org/10.1016/j.cemconres.2020.106307.
[54] J. Skibsted, R. Snellings, Reactivity of supplementary cementitious materials (SCMs) in cement blends, Cem. Concr. Res. 124 (2019), https://doi.org/10.1016/j.cemconres.2019.105799.
[55] T. Matschei, B. Lothenbach, F.P. Glasser, The role of calcium carbonate in cement hydration, Cem. Concr. Res. 37 (2007) 551–558, https://doi.org/10.1016/j.cemconres.2006.10.013.
[56] M. Antoni, Investigation of cement substitution by blends of calcined clays and limestone, EPFL (2013), https://doi.org/10.5075/epfl-thesis-6001.
[57] T.R. Muzenda, P. Hou, S. Kawashima, T. Sui, X. Cheng, The role of limestone and calcined clay on the rheological properties of LC3, Cem. Concr. Compos. 107 (2020), 103516, https://doi.org/10.1016/j.cemconcomp.2020.103516.
[58] M.A.B. Beigh, V.N. Nerella, E. Secrieru, V. Mechtcherine, Structural build-up behavior of limestone calcined clay cement (LC^3) pastes in the context of digital concrete construction, in: Rheol. Process. Constr. Mater, 2019, pp. 1–8.
[59] A. Perrot, D. Rangeard, A. Pierre, Structural built-up of cement-based materials used for 3D-printing extrusion techniques, Mater. Struct. 49 (2016) 1213–1220, https://doi.org/10.1617/s11527-015-0571-0.
[60] Y. Chen, Z. Li, S. Chaves Figueiredo, O. Çopuroğlu, F. Veer, E. Schlangen, Limestone and calcined clay-based sustainable cementitious materials for 3D concrete printing: a fundamental study of extrudability and early-age strength development, Appl. Sci. 9 (2019) 1809, https://doi.org/10.3390/app9091809.
[61] K. Vance, A. Kumar, G. Sant, N. Neithalath, The rheological properties of ternary binders containing Portland cement, limestone, and metakaolin or fly ash, Cem. Concr. Res. 52 (2013) 196–207, https://doi.org/10.1016/j.cemconres.2013.07.007.
[62] R. Sposito, N. Beuntner, K.-C. Thienel, Characteristics of calcined clay particles and their influence on the efficiency of superplasticizers, Cem. Concr. Compos. 110 (2020), 103594, https://doi.org/10.1016/j.cemconcomp.2020.103594.
[63] H. Paiva, A. Velosa, P. Cachim, V.M. Ferreira, Effect of metakaolin dispersion on the fresh and hardened state properties of concrete, Cem. Concr. Res. 42 (2012) 607–612, https://doi.org/10.1016/j.cemconres.2012.01.005.
[64] C. Perlot, P. Rougeau, S. Dehaudt, Slurry of metakaolin combined with limestone addition for self-compacted concrete. Application for precast industry, Cem. Concr. Compos. 44 (2013) 50–57, https://doi.org/10.1016/j.cemconcomp.2013.07.003.
[65] N. Nair, K. Mohammed Haneefa, M. Santhanam, R. Gettu, A study on fresh properties of limestone calcined clay blended cementitious systems, Constr. Build. Mater. 254 (2020), 119326, https://doi.org/10.1016/j.conbuildmat.2020.119326.
[66] NEN-EN 196-2, Method of Testing Cement - Part 2: Chemical Analysis of Cement, 2013.
[67] F. Avet, R. Snellings, A. Alujas Diaz, M. Ben Haha, K. Scrivener, Development of a new rapid, relevant and reliable (R3) test method to evaluate the pozzolanic reactivity of calcined kaolinitic clays, Cem. Concr. Res. 85 (2016) 1–11, https://doi.org/10.1016/j.cemconres.2016.02.015.
[68] D. Marchon, S. Kawashima, H. Bessaies-Bey, S. Mantellato, S. Ng, Hydration and rheology control of concrete for digital fabrication: potential admixtures and cement chemistry, Cem. Concr. Res. 112 (2018) 96–110, https://doi.org/10.1016/j.cemconres.2018.05.014.
[69] ASTM C1506-09, Standard Test Method for Water Retention of Hydraulic Cement-Based Mortars and Plasters. www.astm.org, 2009.
[70] M.K. Mohan, A.V. Rahul, K. Van Tittelboom, G. De Schutter, Extrusion-based concrete 3D printing from a material perspective: a state-of-the-art review, Cem. Concr. Compos. 115 (2020), 103855, https://doi.org/10.1016/j.cemconcomp.2020.103855.
[71] NEN-EN 196-3, Methods of Testing Cement. Part 3: Determination of Setting Times and Soundness, 2016.
[72] Y.W.D. Tay, B. Panda, S.C. Paul, N.A. Noor Mohamed, M.J. Tan, K.F. Leong, 3D printing trends in building and construction industry: a review, Virtual Phys. Prototyp. 12 (2017) 261–276, https://doi.org/10.1080/17452759.2017.1326724.
[73] K. Yu, W. McGee, T.Y. Ng, H. Zhu, V.C. Li, 3D-printable engineered cementitious composites (3DP-ECC): fresh and hardened properties, Cem. Concr. Res. 143 (2021), 106388, https://doi.org/10.1016/j.cemconres.2021.106388.
[74] N. Roussel, Rheological requirements for printable concretes, Cem. Concr. Res. 112 (2018) 76–85, https://doi.org/10.1016/j.cemconres.2018.04.005.
[75] S. Mantellato, M. Palacios, R.J. Flatt, Relating early hydration, specific surface and flow loss of cement pastes, Mater. Struct. Constr. 52 (2019) 1–17, https://doi.org/10.1617/s11527-018-1304-y.
[76] E. Berodier, K. Scrivener, Understanding the filler effect on the nucleation and growth of C-S-H, J. Am. Ceram. Soc. 97 (2014) 3764–3773, https://doi.org/10.1111/jace.13177.
[77] NEN-EN 196-1, Methods of Testing Cement - Part 1: Determination of Strength, 2016.
[78] J.M. Justice, K.E. Kurtis, Influence of metakaolin surface area on properties of cement-based materials, J. Mater. Civ. Eng. 19 (2007) 762–771, https://doi.org/10.1061/(ASCE)0899-1561(2007)19:9(762.
[79] B.H. Zaribaf, K.E. Kurtis, Admixture compatibility in metakaolin–portland-limestone cement blends, Mater. Struct. Constr. 51 (2018) 1–13, https://doi.org/10.1617/s11527-018-1154-7.
[80] M. Palacios, R.J. Flatt, Working Mechanism of Viscosity-Modifying Admixtures, Elsevier Ltd, 2015, https://doi.org/10.1016/B978-0-08-100693-1.00020-5.
[81] C.D. Hatch, J.S. Wiese, C.C. Crane, K.J. Harris, H.G. Kloss, J. Baltrusaitis, Water adsorption on clay minerals as a function of relative humidity: application of BET and Freundlich adsorption models, Langmuir. 28 (2012) 1790–1803, https://doi.org/10.1021/la2042873.
[82] N. Roussel, H. Bessaies-Bey, S. Kawashima, D. Marchon, K. Vasilic, R. Wolfs, Recent advances on yield stress and elasticity of fresh cement-based materials, Cem. Concr. Res. 124 (2019), 105798, https://doi.org/10.1016/j.cemconres.2019.105798.
[83] H. Bessaies-Bey, M. Palacios, E. Pustovgar, M. Hanafi, R. Baumann, R.J. Flatt, N. Roussel, Non-adsorbing polymers and yield stress of cement paste: effect of depletion forces, Cem. Concr. Res. 111 (2018) 209–217, https://doi.org/10.1016/j.cemconres.2018.05.004.
[84] R.J. Flatt, D. Larosa, N. Roussel, Linking yield stress measurements: spread test versus Viskomat, Cem. Concr. Res. 36 (2006) 99–109, https://doi.org/10.1016/j.cemconres.2005.08.001.
[85] A.W. Saak, H.M. Jennings, S.P. Shah, A generalized approach for the determination of yield stress by slump and slump flow, Cem. Concr. Res. 34 (2004) 363–371, https://doi.org/10.1016/j.cemconres.2003.08.005.
[86] H. Huang, T. Huang, Q. Yuan, D. Zhou, D. Deng, L. Zhang, Temperature dependence of structural build-up and its relation with hydration kinetics of cement paste, Constr. Build. Mater. 201 (2019) 553–562, https://doi.org/10.1016/j.conbuildmat.2018.12.226.
[87] F. Dalas, S. Pourchet, D. Rinaldi, A. Nonat, S. Sabio, M. Mosquet, Modification of the rate of formation and surface area of ettringite by polycarboxylate ether superplasticizers during early C3A-CaSO4 hydration, Cem. Concr. Res. 69 (2015) 105–113, https://doi.org/10.1016/j.cemconres.2014.12.007.
[88] J.J. Chen, A.K.H. Kwan, Superfine cement for improving packing density, rheology and strength of cement paste, Cem. Concr. Compos. 34 (2012) 1–10, https://doi.org/10.1016/j.cemconcomp.2011.09.006.
[89] W.W.S. Fung, A.K.H. Kwan, Role of water film thickness in rheology of CSF mortar, Cem. Concr. Compos. 32 (2010) 255–264, https://doi.org/10.1016/j.cemconcomp.2010.01.005.
[90] H. Liu, X. Sun, H. Du, H. Lu, Y. Ma, W. Shen, Z. Tian, Effects and threshold of water film thickness on multi-mineral cement paste, Cem. Concr. Compos. 112 (2020), 103677, https://doi.org/10.1016/j.cemconcomp.2020.103677.
[91] L.G. Li, A.K.H. Kwan, Concrete mix design based on water film thickness and paste film thickness, Cem. Concr. Compos. 39 (2013) 33–42, https://doi.org/10.1016/j.cemconcomp.2013.03.021.
[92] L.G. Li, A.K.H. Kwan, Mortar design based on water film thickness, Constr. Build. Mater. 25 (2011) 2381–2390, https://doi.org/10.1016/j.conbuildmat.2010.11.038.
[93] P. Nanthagopalan, M. Haist, M. Santhanam, H.S. Müller, Investigation on the influence of granular packing on the flow properties of cementitious suspensions, Cem. Concr. Compos. 30 (2008) 763–768, https://doi.org/10.1016/j.cemconcomp.2008.06.005.
[94] H.H.C. Wong, A.K.H. Kwan, Packing density of cementitious materials: part 1-measurement using a wet packing method, Mater. Struct. Constr. 41 (2008) 689–701, https://doi.org/10.1617/s11527-007-9274-5.
[95] G. Gelardi, R.J. Flatt, Working Mechanisms of Water Reducers and Superplasticizers, Elsevier Ltd, 2015, https://doi.org/10.1016/B978-0-08-100693-1.00011-4.
[96] R.J. Flatt, Y.F. Houst, A simplified view on chemical effects perturbing the action of superplasticizers, Cem. Concr. Res. 31 (2001) 1169–1176, https://doi.org/10.1016/S0008-8846(01)00534-8.
[97] J. Plank, Z. Dai, P.R. Andres, Preparation and characterization of new Ca-Al-polycarboxylate layered double hydroxides, Mater. Lett. 60 (2006) 3614–3617, https://doi.org/10.1016/j.matlet.2006.03.070.
[98] D. Marchon, P. Juilland, E. Gallucci, L. Frunz, R.J. Flatt, Molecular and submolecular scale effects of comb-copolymers on tri-calcium silicate reactivity: toward molecular design, J. Am. Ceram. Soc. 100 (2017) 817–841, https://doi.org/10.1111/jace.14695.

[99] R.J. Flatt, Towards a prediction of superplasticized concrete rheology, Mater. Struct. 37 (2004) 289–300, https://doi.org/10.1007/bf02481674.
[100] D. Marchon, R.J. Flatt, Impact of Chemical Admixtures on Cement Hydration, Elsevier Ltd, 2015, https://doi.org/10.1016/B978-0-08-100693-1.00012-6.
[101] A. Zingg, F. Winnefeld, L. Holzer, J. Pakusch, S. Becker, R. Figi, L. Gauckler, Interaction of polycarboxylate-based superplasticizers with cements containing different C3A amounts, Cem. Concr. Compos. 31 (2009) 153–162, https://doi.org/10.1016/j.cemconcomp.2009.01.005.